photonics

MDPI

Review

MOCVD Growth of Next-Generation III–V Semiconductor Devices: In Review

Zoya Noor [1], Muhammad Usman [1,*], Shazma Ali [1], Anis Naveed [1], Amina Hafeez [2] and Ahmed Ali [3,*]

[1] Faculty of Basic Sciences, Ghulam Ishaq Khan Institute of Engineering Sciences and Technology, Topi 23460, Pakistan
[2] Department of Physics, Abbottabad University of Science and Technology, Abbottabad 22010, Pakistan
[3] Biomedical and Instrument Engineering Program, College of Engineering and Energy, Abdullah Al Salem University, Khaldiya, Kuwait City 72303, Kuwait
* Correspondence: m.usman@giki.edu.pk (M.U.); ahmed.ali@aasu.edu.kw (A.A.)

Abstract

Metal–organic chemical vapor deposition (MOCVD) is a crystal growth technique used to achieve high-purity thin films, especially III–V materials, for fabricating semiconductor devices. It allows for thickness tunability, controlled doping, and composition of epilayers. This review focuses on the principle of MOCVD, its historical background, and its applications in III–V semiconductor devices such as solar cells, high electron mobility transistors (HEMTs), light-emitting diodes (LEDs), laser diodes (LDs), and photonic integrated circuits (PICs). This review highlights the recent developments in MOCVD aimed at improving its efficiency, performance, and sustainability. Finally, we emphasize emerging trends and challenges in MOCVD process innovation, reactor design, and material integration that are poised to drive the development of next-generation optoelectronic, photonic, and quantum technologies. Together, these findings underscore MOCVD's pivotal role in enabling high-performance devices and sustaining leadership in post-Moore semiconductor technologies.

Keywords: metal–organic chemical vapor deposition; solar cell; LED; HEMT; laser diodes; PICs

1. Introduction

Semiconductor advances are increasingly shaped by breakthroughs in materials engineering, particularly as the semiconductor industry approaches the limits of Moore's law [1,2]. As an evolving technology, metal–organic chemical vapor deposition (MOCVD) has turned into a famous scalable manufacturing technique for the fabrication of next-generation electronics and photonics. The advantages of MOCVD, like excellent control over doping, composition, temperature, and growth factors, have made it possible to fabricate complex structures, including III–V multi-junction solar cells, GaN-based electronics, micro-light-emitting diodes (LEDs), and nano-LEDs [3–7]. Furthermore, the inherent scalability, uniformity, and industrial benefits of MOCVD facilitate its progression from laboratory-scale demonstrations to large-scale industrial production. It is also used for novel applications, including heterogeneous photonic integration and optical quantum technologies [8–10].

MOCVD is widely regarded as a leading technique for the epitaxial growth of III–V semiconductors because it provides exceptional control over composition, layer thickness, doping, and interface quality. In multi-junction solar cells, MOCVD facilitates precise deposition of lattice-matched, strain-balanced layers, such as InGaP/InGaAs or GaAsP/Ge,

Check for updates

Received: 25 December 2025
Revised: 6 March 2026
Accepted: 10 March 2026
Published: 12 March 2026

Copyright: © 2026 by the authors. Licensee MDPI, Basel, Switzerland. This article is an open access article distributed under the terms and conditions of the Creative Commons Attribution (CC BY) license.

thereby providing high-efficiency devices with uniform light absorption and reduced defects at tunnel junctions [11]. For laser diodes (LDs) such as InP quantum dot lasers and AlGaInP/GaInP visible lasers, MOCVD enables precise control over quantum well and quantum dot growth, uniform carrier confinement, and consistent emission wavelengths, which are essential for achieving low threshold current densities and high output power [12,13]. In LEDs, MOCVD enables conformal growth on complex device geometries and facilitates high-quality sidewall passivation, as demonstrated in micro-LEDs, thereby enhancing external quantum efficiency and device reliability [14]. For high electron mobility transistors (HEMTs), MOCVD enables the formation of sharp heterointerfaces and precise control of AlGaN/GaN composition, which are essential for achieving high two-dimensional electron gas (2DEG) mobility and high breakdown voltage [15]. In photonic integrated circuits (PICs), MOCVD permits the monolithic integration of multiple active and passive components, including lasers, modulators, and detectors, with precise control over layer uniformity and optical confinement, thereby supporting scalable and reliable photonic platforms [16]. Overall, the versatility, reproducibility, and scalability of MOCVD make it an indispensable technique for fabricating advanced optoelectronic and electronic devices, offering industrial relevance and technical precision that are difficult to achieve with other deposition methods [17].

In addition to MOCVD, some other techniques are used for material deposition such as molecular beam epitaxy (MBE), chemical bath deposition (CBD), atomic layer deposition (ALD), sputtering, and thermal evaporation [18]. MBE is a highly refined technique that offers atomic-scale precision during thin film growth. A very high vacuum is required in the MBE chamber, where the evaporated material is deposited in the form of a thin film by condensation on the substrate. In comparison to MOCVD, MBE features lower growth rates, incurs higher costs due to the need for continuous ultra-high vacuum, and offers less flexibility in precursor chemistry, which complicates the growth of certain alloys. This is particularly evident in the poor compatibility of MBE with phosphorus a high-vapor-pressure element that is challenging to manage in an ultra-high voltage (UHV) environment [19,20]. CBD uses an aqueous solution with precursor ions, and the thin film deposition process occurs by a chemical reaction when the substrate is dipped into this solution. Compared to the MOCVD process, CBD has very little control over layer deposition and a higher chance of defects in the film [21]. ALD builds thin films by successive layer deposition and enables the fabrication of thin films, which are further used in multiple applications. ALD is preferable for ultra-thin layer deposition applications, but MOCVD remains the dominant technique for industrial use, as ALD shows some limitations related to throughput, scalability, and cost for high-volume manufacturing [22]. Another known deposition technique, named sputtering, uses a vacuum chamber and energetic ions that bombard the target material, resulting in atom ejection, which is further deposited on the substrate layer. MOCVD offers precise control over composition and growth conditions, enabling the deposition of high-quality films, especially for compound semiconductors, whereas sputtering is generally more suitable for metallic or amorphous thin films [23]. Thermal evaporation uses a vacuum chamber, and the targeted material evaporates and is then followed by a condensation process onto the substrate surface. Poor stoichiometric control and lower scalability of thin films made this technique not very appropriate for industrial usage [24]. Some alternative terms used for MOCVD are Metal–Organic Vapor Phase Epitaxy (MOVPE), Metal–Organic Vapor Deposition (MOVD), and Organometallic Vapor Phase Epitaxy (OMVPE) [25–28]. Table 1 shows a summarized comparison of the growth techniques for the fabrication of modern optoelectronic devices.

Table 1. Comparison of the growth techniques for fabricating optoelectronic devices.

Growth Technique	Deposition Mechanism	Material Quality	Thickness Control	Typical Applications in Optoelectronics	Advantages	Limitations
MOCVD	Chemical reaction of metal–organic precursors in vapor phase	High crystalline quality (epitaxial)	Moderate to high (nm–µm scale)	III–V LEDs, LDs, HEMTs, quantum wells, distributed Bragg reflectors (DBRs), VCSELs	Scalable, industry standard for III–Vs, good uniformity	Complex precursor handling, toxic precursors, high temperature, expensive setup
MBE	Physical evaporation in ultra-high vacuum with atomic beams	Ultra-high purity and atomic precision	Excellent (monolayer control)	Quantum dots, superlattices, low-dimensional heterostructures, quantum photonic devices	Precise control, low defect density, in situ monitoring (RHEED)	Slow growth rate, costly, limited scalability
CBD	Chemical reaction in aqueous solution at low temperature	Polycrystalline or amorphous	Poor (µm scale, non-uniform)	Buffer layers, window layers in solar cells, low-cost photodetectors	Simple, low-cost, low temperature	Poor film quality, limited to certain materials
ALD	Sequential self-limiting surface reactions	Conformal, pinhole-free films	Excellent (angstrom-level)	Passivation layers, tunnel barriers, dielectric coatings, nanophotonic structures	Atomic precision, excellent step coverage, low defect density	Slow throughput, limited material choices for optoelectronics
Sputtering	Physical ejection of atoms via ion bombardment	Dense, uniform films	Good (nm–µm scale)	Transparent conductive oxides (TCOs), metal contacts, dielectric mirrors	Versatile, good adhesion, scalable	May induce damage, less suitable for epitaxy
Thermal Evaporation	Heating source material to vaporize in vacuum	Moderate (depends on substrate)	Fair (nm–µm scale)	Metal electrodes, organic layers, simple photodetector structures	Simple setup, fast deposition	Poor step coverage, limited control over stoichiometry

In MOCVD, thin-film growth occurs when the substrate is exposed to gaseous precursors, enabling the deposition of high-quality semiconductor layers. The MOCVD chamber is shown in Figure 1, in which precursor gases for indium, gallium, and phosphorus are purged to make III–V films. For this deposition, MOCVD uses trimethylgallium (TMGa), trimethylindium (TMIn), and phosphine as precursor gases, and the gases undergo a pyrolysis process and are deposited on the substrate to produce a thin film. Byproducts like methane and hydrogen are removed from the chamber. A low-pressure vacuum ranging from 10 torr to 100 torr is maintained in the reaction chamber [29,30].

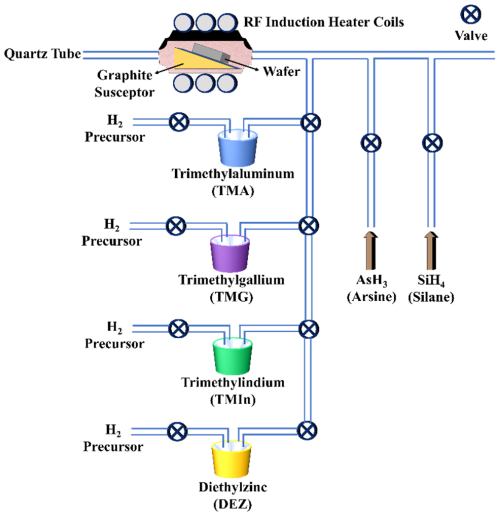

Figure 1. MOCVD chamber. Adapted from Ref. [31].

The reactions are shown here:

$$In(CH_3)_3 \rightarrow In + 3CH_3$$

$$Ga(CH_3)_3 \rightarrow Ga + 3CH_3$$

$$2PH_3 \rightarrow 2P + 3H_2$$

$$xIn + (1-x)P + Ga \rightarrow In_xGa_{(1-x)}P$$

The objective of this review is to introduce the significance of MOCVD in the fabrication and design of optical and electronic devices. Furthermore, it includes the mechanism of the MOCVD chamber, the historical timeline of MOCVD (Figure 2), the contribution, and the favorable outcomes of using MOCVD in device fabrication. MOCVD was first used in the late 19th century for the deposition of semiconductor compounds on the substrate [32]. In 1968, MOCVD was first utilized [33] to deposit semiconductor compounds with metal organics and hydride precursors [34]. In 1972, GaAs was grown as a single crystal by utilizing trimethylgallium and arsine in the MOCVD chamber [35]. Further, GaP and GaAs films have also been grown [36,37]. II–VI compounds have also been grown using MOCVD [38]. Electronic devices such as LEDs, solar cells, and HEMTs have been made using MOCVD ever since its success. MOCVD has enabled significant breakthroughs in device development through the creation of multi-quantum wells and heterostructures [39–41]. In 1990, the biggest breakthrough happened when gallium nitride (GaN) thin films were successfully grown via MOCVD. In 1993, the first blue LED was commercialized as indium gallium nitride InGaN/GaN multi-quantum well structures were successfully grown by MOCVD [42].

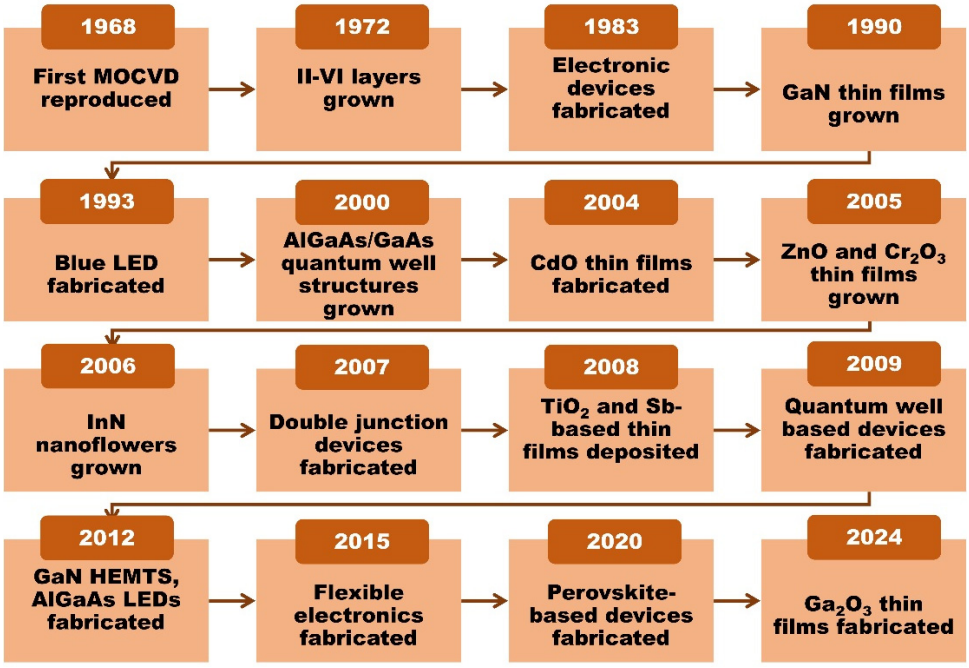

Figure 2. Historical timeline of MOCVD in device fabrication.

AlGaAs/GaAs quantum well structures have been made via MOCVD. These structures have been utilized to make efficient solar cells, laser diodes, LEDs, and HEMTs [43,44]. In 2005, MOCVD was reportedly used to grow zinc oxide (ZnO) and Cr_2O_3 thin films. ZnO thin films have been grown using dimethylzinc and water or oxygen as precursors, and the substrates used are silicon, glass, and sapphire, based on the application

of the device [45,46]. In 2006, the MOCVD growth of indium nitride (InN) nanoflowers revolutionized nitride semiconductor research due to their unique morphology and previously unattainable optoelectronic properties [47]. Further, rare-earth oxides have been grown via MOCVD. InGaN-based transistors have also been grown successfully [48–50]. In 2007, significant modifications to the MOCVD reactor design enabled the successful fabrication of dual- and triple-junction solar cells, achieving 15–20% higher power conversion efficiencies compared to conventional single-junction devices. In 2008, In_2S_3, TiO_2, and antimonide-based thin films were deposited via this technology [51,52]. In 2009, quantum well laser diodes, UV photodetectors, and ZnO nanowires were fabricated by MOCVD [53]. Advanced MOCVD reactors made by Veeco, AIXTRON, and Taiyo Nippon Sanso brought significant improvements in layer deposition, process effectiveness, and budget-friendly fabrication [54,55]. Quantum dots and nanostructures have been fabricated by MOCVD [56,57]. Flexible electronics and micro-LEDs have been fabricated using MOCVD as well. Fabrication of needle-shaped tunnel junction contacts on micro-LEDs using a hybrid growth approach combining plasma-assisted molecular beam epitaxy (PA-MBE) and MOCVD has been demonstrated [14]. The contacts incorporated an ultra-thin InGaN polarization layer, which enabled a steep doping interface and facilitated an efficient interband tunneling effect. This engineered structure exhibited significantly reduced series resistance and superior current scaling performance compared to conventional micro-LED designs. Thin titanium dioxide (TiO_2) films are deposited on patterned silicon (Si) and silicon nitride (SiN) substrates using pulsed-pressure metal–organic chemical vapor deposition (PP-MOCVD) [58]. A CdHgTe (CMT) infrared detector in medium and long wavelength regions has been grown using MOCVD with a quantum efficiency of up to 65% [59]. Perovskite/III–V and III–V/Si tandem solar cells have also been fabricated via MOCVD [60]. Temperature-sensitive materials like perovskite have also been fabricated with a customized low-temperature growth MOCVD reactor [61]. In 2024, Ga_2O_3 thin films were grown via MOCVD [62]. Additionally, GaN nanowire nanogenerators, with an output power density around ~12.5 mW/m^2, have also been reported [63]. Therefore, continued progress in MOCVD processes, reactor engineering, and precise growth control is directly linked to maintaining strategic leadership in state-of-the-art semiconductor devices [64].

2. MOCVD-Grown Next-Gen Devices

2.1. Solar Cells

The solar cell operates by converting incident photons into electricity via the photovoltaic effect, wherein absorbed photons generate electron–hole pairs that are then separated and driven through an external circuit to produce a current. French physicist Alexandre-Edmund Becquerel discovered the photovoltaic effect in 1839 while working on an electrolytic cell [65]. The first practical solar cell, created by Charles Fritts in 1883, used a selenium wafer coated with gold, achieving a low conversion efficiency of approximately 1–2% [66]. Early progress continued into the mid-20th century. The development of high-purity single-crystal silicon using the Czochralski process enabled researchers, most notably at Bell Labs in 1954, to achieve ~6% efficiency [67]. To produce high-purity silicon crystals, the Czochralski process was developed in the early 20th century enabling silicon solar cells with efficiency of 11%. Today, a diverse array of materials is being explored to push solar conversion efficiencies even higher. Monocrystalline silicon cells have reached record efficiencies of 26.7% [68]. Multicrystalline silicon solar cell efficiencies of up to 22% have been reported [69]. Polycrystalline CdTe solar cells have exceeded 20% efficiency [70]. III–V semiconductor multi-junction cells, especially under concentrator systems, have surpassed 30% efficiency [71]. Perovskite solar cells currently exceed 25% efficiency, rapidly closing the gap with crystalline silicon [72]. Organic photovoltaics show

efficiencies up to 18%, with advantages in flexibility and low-cost manufacturing. Over 95% of the global solar photovoltaic (PV) market is currently dominated by crystalline silicon (c-Si) technologies, primarily due to their high efficiency, reliability, and cost-effectiveness. Today, researchers test materials such as single-crystal silicon, polycrystalline silicon, III–V compounds, perovskites, and organic semiconductors for solar cell fabrication, achieving significantly higher efficiencies [73–78].

2.1.1. Challenges

During the growth of solar cells via MOCVD, challenges like purity of material, process control, proper interface formation, and cost-effectiveness are faced. The major issue faced is lattice mismatching, incorporation of impurities, or defects, which can reduce the efficiency of a solar cell. Generally, III–V semiconductor compounds, when grown on different substrates or multi-junction solar cells, face lattice mismatch issues, which result in defect creation that reduce the movement of electrons and holes. The flow rate of precursor gases must be managed; otherwise, non-uniform doping, poor junction formation, and defects are caused. The high cost of the MOCVD reactor is a major challenge while trying to commercialize these solar cells. Also the precursor gases (e.g., trimethylindium) used are of high purity (e.g., arsine, phosphine) and, thus, costly. Factors such as maintaining chamber cleanliness to prevent impurity incorporation, utilizing high-purity precursors, precisely controlling growth environment parameters (temperature, pressure, flow rates), and ensuring stringent thickness and compositional uniformity across the wafer are mandatory for the fabrication of high-quality solar cells devices via MOCVD [17,79–81]. These stringent growth requirements limit the application of III–V solar cells to high-value applications like space satellites and concentrated photovoltaics. Furthermore, growing high-efficiency devices on low-cost, lattice-mismatched substrates like silicon require sophisticated buffer layer engineering to mitigate threading dislocations, which act as recombination centers and degrade performance. While MBE offers atomic precision, it is too slow and costly for large-scale solar cell production. In contrast, HVPE is excellent for growing thick GaN substrates but lacks fine control for complex multi-junction structures. However, MOCVD strikes the best balance between precision, complexity, and scalability, making it the dominant method for high-efficiency III–V solar cells used in space and concentrator photovoltaics.

2.1.2. Epitaxial Growth of Solar Cells by MOCVD

MOCVD has been utilized to fabricate single-junction germanium solar cells with a GaAs substrate, as shown in Figure 3. A Ge solar cell has been grown on a Si substrate using MOCVD [82]. For growing layers of GaAs, InGaP, and Ge, the precursors used are trimethylgallium, trimethylindium, arsine, phosphine, and isobutylgermane. The dopant sources used here are trimethylgallium (for p-type Ge) and silane (for n-type InGaP and GaAs). The carrier gas used in the MOCVD chamber is hydrogen, and the pressure is kept at 100 millibars. The growth of the p-type Ge layer is done at 600 °C, and during the fabrication of other layers, the temperature is set at 670 °C. Different flow rates of dopant source gases are used to reduce the dopant concentration. Solar cells A, B, and C are the ones in which GaAs is used as a substrate. For reference, for solar cell D, the substrate is Ge. The base layer thickness is set at 1 µm, and the doping concentration is 4×10^{19} and 2×10^{18} for solar cells A and B. For solar cell C, the base layer thickness is set at 5 µm, and the doping concentration is set at 2×10^{18}. For the first time, a Ge solar cell is grown on a GaAs substrate, and a discontinuous doping technique is employed to reduce the doping concentration. In the discontinuous doping technique, dopant incorporation is modulated during MOCVD growth such that dopant supply is applied intermittently rather than continuously [83]. The current–voltage (IV) curve and external quantum efficiency (EQE)

versus wavelength are shown in Figure 3b,c. Solar cell C has better results in terms of current density and EQE as compared to solar cell A and solar cell B, which are observed clearly in Figure 3b,c. In Figure 3b, solar cell A, solar cell B, and solar cell C have a current density of 26.21 mA/cm^2, 36.64 mA/cm^2, and 42.96 mA/cm^2, respectively. Open circuit voltage (V_{oc}) values are 0.22 V, 0.28 V, and 0.24 V for solar cell A, solar cell B, and solar cell C respectively. Furthermore, the EQE curve shows that solar cell C has a peak EQE value of 85% at wavelengths 700 to 900 nm. Solar cell A and solar cell B have lower peak EQE values when compared with solar cell C. Solar cell B has reported the highest efficiency and fill factor (FF) of 6.72% and 65.4% while solar cell A has an efficiency of 2.87% and FF of 49.83%, whereas solar cell C has an efficiency and FF of 6.57% and 63.7% [83].

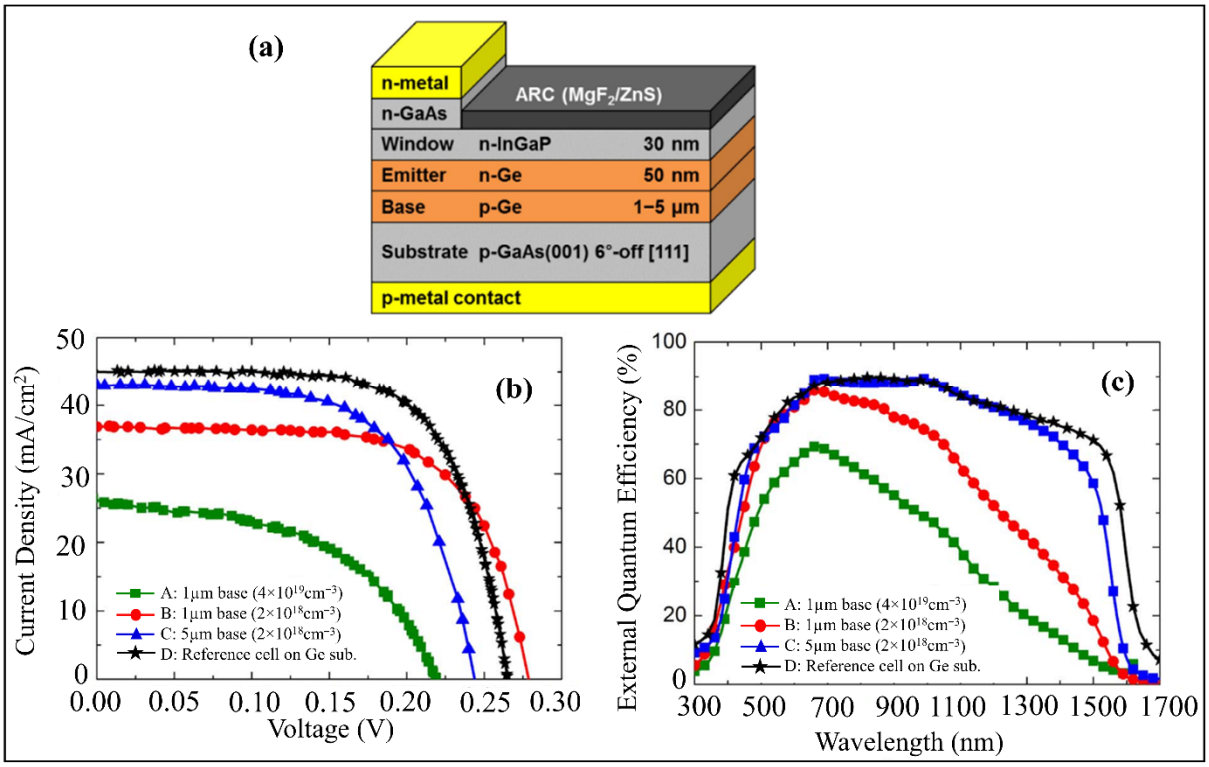

Figure 3. (**a**) Illustration of a Ge solar cell grown by MOCVD, (**b**) current density versus voltage curve, and (**c**) external quantum efficiency versus wavelength. Reproduced with permission from Ref. [83].

The dual junction $GaAs_{0.75}P_{0.25}$/Si solar cell was fabricated experimentally using two approaches: (i) by MOCVD and (ii) hybrid MOCVD-MBE. The structure of GaAsP/Si is shown in Figure 4a. The precursors employed in MOCVD are trimethylaluminum, triethylgallium, trimethylgallium, trimethylindium, phosphine (PH_3), tert-Butylphosphine (TBP), arsine (AsH_3), and silane (SiH_4). The n-type doping of the buffer and cell layer is done by silane. p-type doping is done by diethylzinc (DEZn, $(C_2H_5)_2Zn$). For tunnel junction fabrication, the dopants employed are Diethyl telluride (DETe, $(C_2H_5)_2Te$) and bromotrichloromethane ($CBrCl_3$). For MBE growth, Si and Be are used for n-type and p-type doping. Two different samples are grown, named sample I and sample II. In sample I, all layers are grown via MOCVD while in sample II, the bottom cell is grown via MOCVD and the top cell and the tunnel junction are grown via MBE. After comparing the results of both techniques, it is observed that MOCVD is better for the fabrication of such devices, as sample I exhibited superior performance among them. The improved performance of the MOCVD sample I compared to the MOCVD-MBE sample II is primarily driven by using a single epitaxial growth technique, which results in enhanced interface quality and reduced

defect formation. The hybrid MOCVD-MBE approach proposes additional interfaces and growth interruptions that can increase recombination losses and degrade carrier transport, resulting in lower device performance. Two different measurement setups of light intensity voltage (LIV) and J_{SC}-V_{OC} are used to compare the results of the devices. A Xenon arc lamp-based simulator named OAI TriSol (OAI, San Jose, CA, USA) with AM1.5G spectrum is used for light current–voltage (LIV) measurement, and the intensity of the lamp is set using a reference solar cell. The same setup along with density filters is used during the calculation of the J_{SC}-V_{OC} setup. The current density versus voltage curve is shown in Figure 4b, and it can be observed that the J_{SC} and V_{OC} values of the device fabricated by MOCVD are better. Using the LIV and J_{SC}-V_{OC} measurement setups, the current densities of sample I and sample II are shown in red and blue in Figure 4b, respectively. Sample I shows a current density of 10.2 mA/cm^2 and V_{OC} of 1.62 V. Sample II shows a current density of 8.6 mA/cm^2 and V_{OC} of 1.52 V [84].

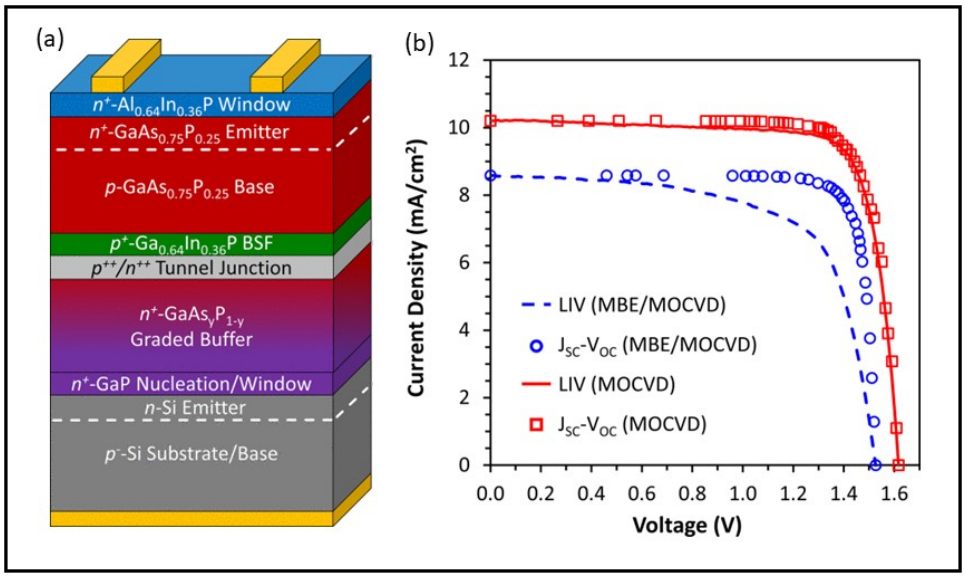

Figure 4. (**a**) Illustration of GaAsP/Si dual junction solar cell, and (**b**) current density versus voltage curve. Reused under creative common license [84].

Different techniques have been used to fabricate Copper Indium Selenide (CIS) solar cells, including co-evaporation [85], sputtering [86], and electrodeposition [87]. These solar cells involve complicated multistep processes, which make them highly overpriced. There are different layers of CIS solar cells named absorbers, buffers, electrodes, and window layers, which require different deposition temperatures and at times different techniques. To resolve this issue, MOCVD is employed to fabricate CIS solar cells [88]. CIS solar cells fabricated by using MOCVD are discussed as follows. The glass substrate coated with molybdenum (Mo) is used as the back contact layer. The next step is to deposit In_xSe_y films by using the precursors named trimethylindium and dimethyldiselenide (DMDSe). Next, a layer of copper (Cu) is deposited by using a precursor gas, hexafluoroacetylacetonato (hfac) copper. The next step is to deposit an InSe layer as deposited previously using the precursors. Next, there is a deposition of Zn(S,O) buffer layer and the boron-doped zinc oxide (ZnO:B) window layer. The buffer layer is a thin layer of zinc sulphide (ZnS) deposited on a zinc oxide layer. The precursors used for both layers are diethylzinc, water (H_2O), tert-Butylthiol (TBT, $(CH_3)_3CSH$), and diborane (B_2H_6) for zinc (Zn), oxygen (O_2), sulphur (S), and boron (B). The structure of the CIS solar cell is shown in Figure 5a. The current density–voltage (J-V), power density–voltage (P-V), and quantum efficiency versus

wavelength curves are shown in Figure 5b,c. The efficiency and the fill factor of CIS-based solar cells are 10.45% and 60.3% [89,90].

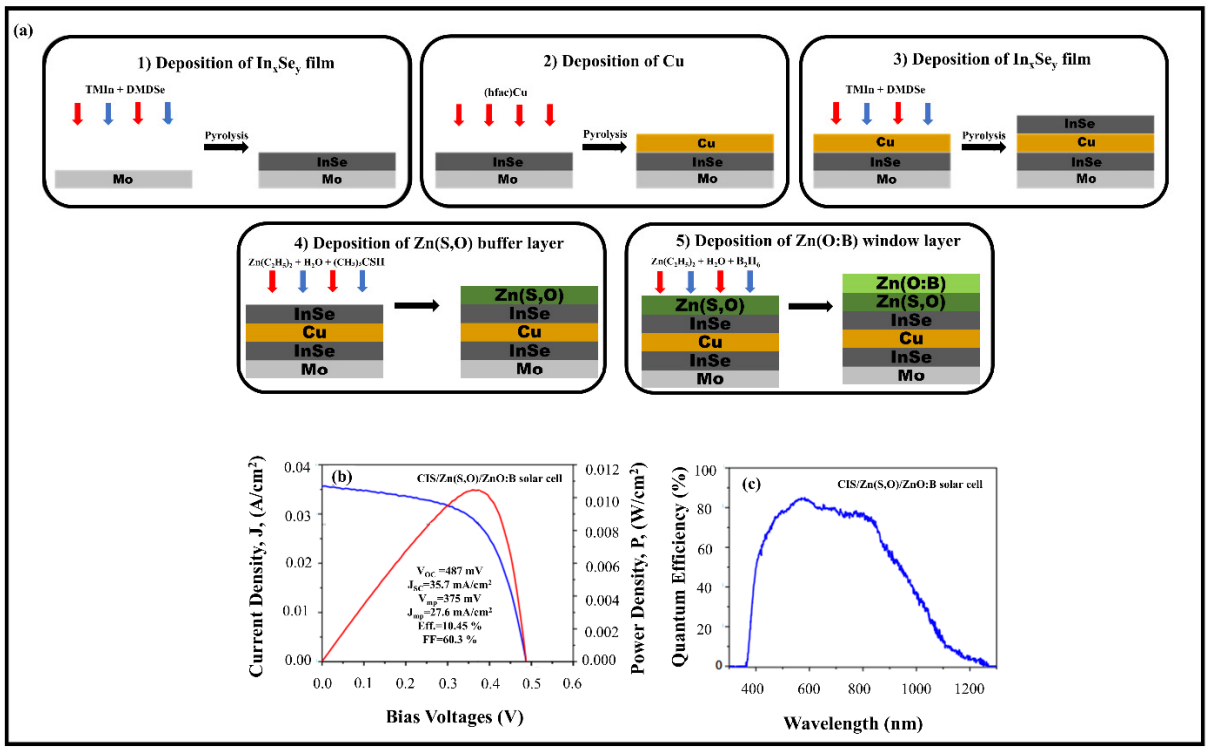

Figure 5. (**a**) Step-by-step MOCVD layer growth of CIS solar cell. Reused under creative common license [90]. (**b**) Current density and power density versus voltage curve, and (**c**) quantum efficiency versus wavelength curve. Reproduced with permission from Ref. [89].

High-performance solar cells have been fabricated via the MOCVD technique, as stated in several studies. The first study shows the growth of Ge solar cells on a GaAs substrate, which shows that this technique offers control over layer thickness and composition. The next study shows that dual junction solar cells grown by MBE and MOCVD techniques, illustrating that MOCVD takes the lead as a uniform, lattice-matched structure is formed. Further, another device named CIS solar cell has been fabricated that shows high quality and uniform thin films ideal for photovoltaic applications. Some of the advantages, as shown by these studies, have excellent control over thickness and composition, high-performance multi-junction devices, and commercial-scale growth. Some of the disadvantages are high cost, toxic precursor gases, and sensitive growth factors, which can result in imperfection if not controlled properly.

2.2. HEMTs

HEMTs exploit the principles of modulation doping and heterojunction band engineering to create a two-dimensional electron gas (2DEG) at the interface of two semiconductor materials, typically a wide bandgap barrier (e.g., AlGaN) and a narrow bandgap channel (e.g., GaN or GaAs). This 2DEG exhibits exceptionally high electron mobility due to spatial separation of charge carriers from ionized impurities, minimizing scattering and enabling ultra-fast carrier transport [91–93]. Due to their high cutoff frequencies, low noise figures, high breakdown voltages, low on-resistance, thermal stability, and radiation hardness, HEMTs are deployed in high frequency and millimeter-wave electronics, electric vehicles, power electronics, and photonic receivers and modulators [94]. Takashi Mimura and Satoshi Hiyamizu produced the first HEMT in 1980 at Fujitsu Laboratories in Japan,

observing high-speed carrier transport [95,96]. The typical structures of GaAs and GaN HEMTs are shown in Figure 6. They consist of a GaAs-based substrate layer, which is semi-insulating. Then, a p-doped GaAs layer is grown, and the next layer is an undoped GaAs channel. Next, an undoped AlGaAs spacer layer is grown. Next, a heavily doped n^+-AlGaAs layer is employed. Further, a lightly doped n-AlGaAs is placed. On top of that, a heavily doped n^+-GaAs layer is present. Further, source, drain, and gate contacts are employed on top of the device. A 2DEG interface is created at AlGaAs (spacer)/GaAs (channel), and electrons are collected at this interface. HEMT blocks the flow of electrons when negative voltage (relative to the source) is applied at the gate and the 2DEG density, thus, decreases. HEMT enhances the flow of electrons when positive voltage (relative to the source) is applied at the gate and the 2DEG density, thus, increases. The gate voltage, thus, controls the flow of current in the HEMT [91,97]. GaN HEMTs offer significantly higher power density (typically 5×–10×) than GaAs HEMTs. For the same output power, a GaN HEMT die is much smaller than a GaAs HEMT die. Table 2 shows the comparison of the two HEMTs.

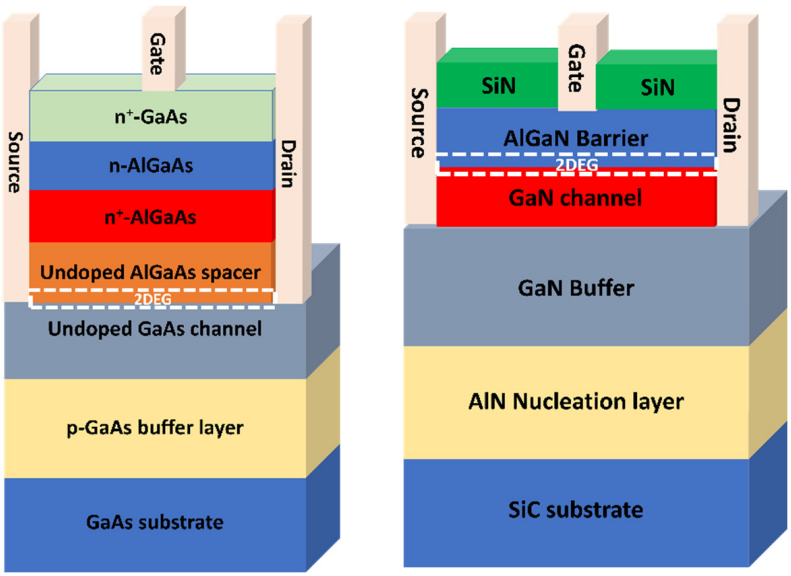

Figure 6. Typical GaAs and GaN HEMTs. Adapted from Refs. [98,99].

Table 2. Typical GaAs HEMT vs GaN HEMT comparison [100–102].

Parameter	GaN HEMT	GaAs HEMT
RF Power Density (W/mm)	5–10	0.5–1
Breakdown Voltage (V)	100–200	20–40
Electron Saturation Velocity (cm/s)	2.5×10^7	1×10^7
Critical Electric Field (MV/cm)	~3.5	~0.3
Operating Temperature (°C)	>300 °C	~150 °C
Power Added Efficiency (PAE)	50–70%	35–50%

2.2.1. Challenges

The development of next-generation power-efficient devices holds great promise. The crystal development process of bulk GaN is very challenging. GaN substrates typically exhibit a defect density ranging from 10^4 to 10^6/cm^2 [103,104]. Fabrication of HEMT by MOCVD faces challenges such as flow rate and purity of precursor gases and growth conditions. A sharp 2DEG interface must be built to enhance the performance of the device. The device reliability and mobility of electrons are hindered by defects within the device, like threading dislocations, impurities, and grain boundaries. Impure precursor gases

can cause contamination, which can affect the quality of the device as well as surface morphology. Current collapse arises from charge trapping in surface and buffer states that deplete the 2DEG under high electric fields, reducing the device output current and power. This necessitates effective surface passivation layers (e.g., SiN), the optimization of which is a major focus of current MOCVD process research [105,106]. In commercial or industrial production, the uniform thickness of different layers and optimal material composition across a large wafer is a significant challenge. To decrease surface traps, defects, impurities, and leakage currents, effective passivation of the device is essential [104,105,107–109]. Despite these challenges, in comparison to other growth methods, MOCVD remains the widely adopted method for growing GaN HEMTs due to its high throughput, precise compositional control, scalability, and compatibility with industry standard processes, ensuring efficient 2DEG formation for high-frequency performance.

2.2.2. Epitaxial Growth of HEMTs by MOCVD

AlGaN/GaN HEMTS are fabricated via MOCVD, and a step-by-step process is shown here in detail in Figure 7. Firstly, an undoped aluminum nitride (AlN) nucleation layer is deposited, as shown in Figure 7a, then a gallium nitride (GaN) channel layer and an AlN spacer layer are deposited on top of each other, as shown in Figure 7b,c, respectively. Next, an aluminum gallium nitride (AlGaN) barrier layer is deposited as shown in Figure 7d. Next, a highly doped GaN cap layer is deposited as depicted in Figure 7e. Next, reactive ion etching (RIE) is used for creating openings for ohmic contacts for the source and drain, as illustrated in Figure 7f. Figure 7g shows that the electron beam evaporation technique is used to deposit a Ti/Al/Ni/Au multi-layer which acts as an ohmic contact. The drain and source contacts are the ohmic contacts. Figure 7h illustrates the RIE process used to etch and create a Schottky contact between the gate and the barrier. Electron beam resist coating is applied. Figure 7i depicts that the electron beam resist layer is removed to develop the area for the formation of the gate. The GaN cap layer is etched to form a gate as shown in Figure 7j. At this stage of fabrication, Figure 7k depicts that the device is ready for gate metal deposition. Now, metal is deposited to form a gate. The metal (Ti/Au) is deposited as a gate, as Figure 7l illustrates. The resist layer and extra metal layers are lifted off as the last step depicted in Figure 7m [110]. In this structure, two different gate lengths, 250 nm and 500 nm, have been tested. Different parameters, such as the drain-to-source current versus drain-to-source voltage curve, the drain-to-source current versus gate voltage curve, the transconductance, and noise analysis, have been measured for various gate lengths. As a result, a 250 nm gate length shows better results. This high-quality epitaxial structure directly contributes to the observed device performance, including a maximum drain current of approximately 1130 mA/mm and 1272 mA/mm for gate lengths of 500 nm and 250 nm, respectively. In this work, the AlGaN/GaN high electron mobility transistor structure, including the AlN nucleation layer, GaN channel, AlN spacer, AlGaN barrier, and GaN cap, are epitaxially grown using MOCVD, which ensured abrupt heterointerfaces, precise control of composition and dopant incorporation, and high crystal quality. The high structural quality achieved via MOCVD is critical for the formation of a high-mobility two-dimensional electron gas (2DEG) at the AlGaN/GaN interface, a key factor underlying the low noise and high-frequency device performance analyzed in this work [110].

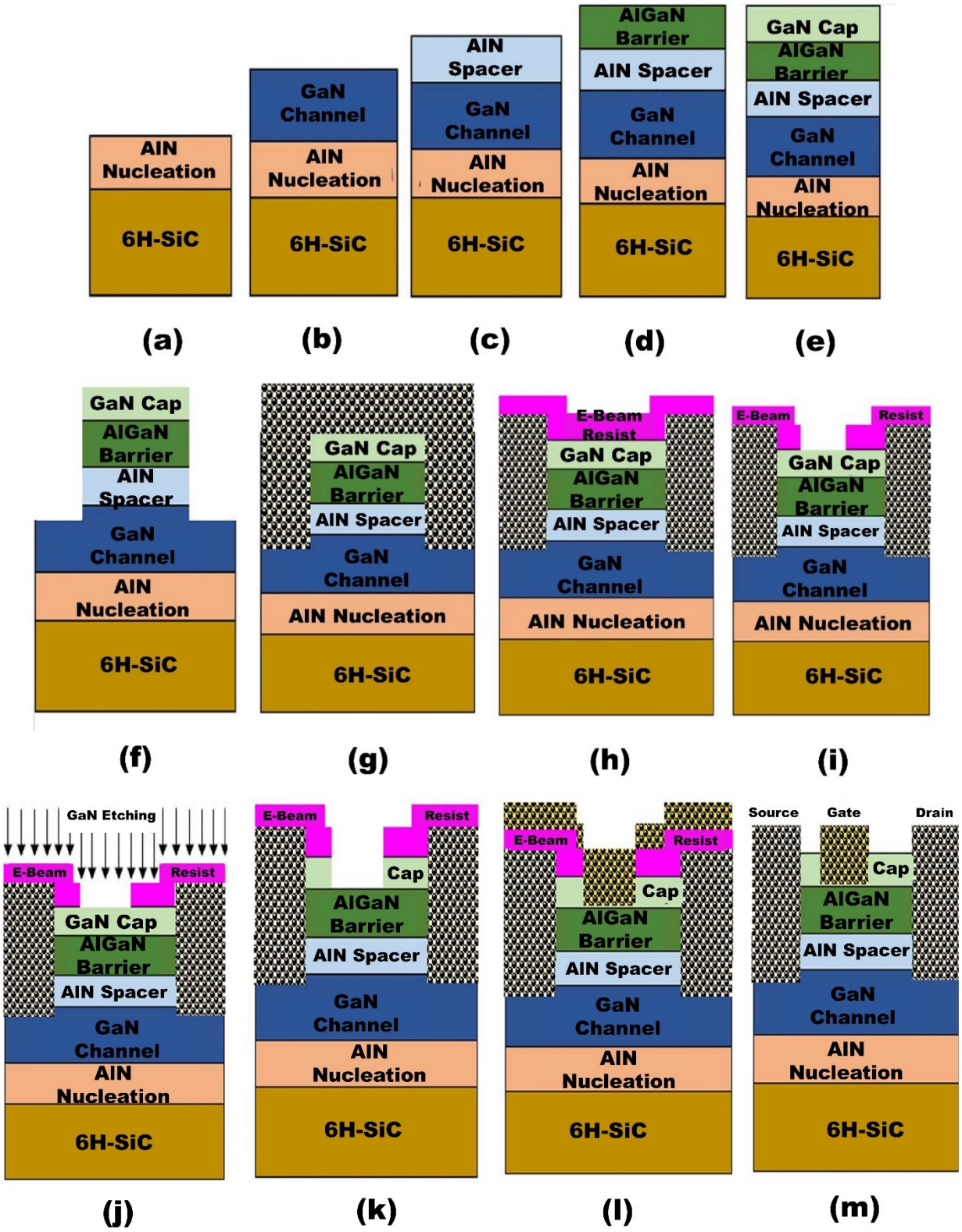

Figure 7. Step-by-step fabrication procedure of AlGaN/GaN HEMT via MOCVD. (**a**) Deposition of AlN layer, (**b**) deposition of GaN layer, (**c**) deposition of AlN layer, (**d**) deposition of AlGaN layer, (**e**) deposition of GaN layer, (**f**) mesa etching over GaN layer, (**g**) ohmic contact deposition, (**h**) deposition of resist layer, (**i**) patterning of the resist layer, (**j**) GaN layer etching, (**k**) defining gate area by development process, (**l**) deposition of gate layer, and (**m**) final structure achieved after doing lift-off procedure. Reused under creative common license [110].

Another HEMT structure is grown on silicon carbide (SiC) substrate by both MOCVD and MBE techniques and the results are compared [111]. Firstly, an AlN nucleation layer, then a GaN buffer layer succeeded by 2DEG channel layer are employed. A 3 to 6 nm thick AlN barrier layer is used. A GaN cap layer with thicknesses ranging from 1 to 4 nm is employed. The schematic is shown in Figure 8. MBE is used to fabricate the device and the source used for nitrogen is UNI-Bulb RF-plasma. The MBE fabrication is done at 730 °C temperature. To grow the same structure by MOCVD, an AIXTRON 2800 G4 HT IC multi-wafer reaction chamber (AIXTRON SE, Herzogenrath, Germany) is utilized. A growth rate of 5 Å s^{-1} and temperature of 1120 °C are used to grow the GaN buffer layer. The growth rate of 0.47 Å s^{-1} and temperature of 1150 °C are used to grow the AlN barrier layer.

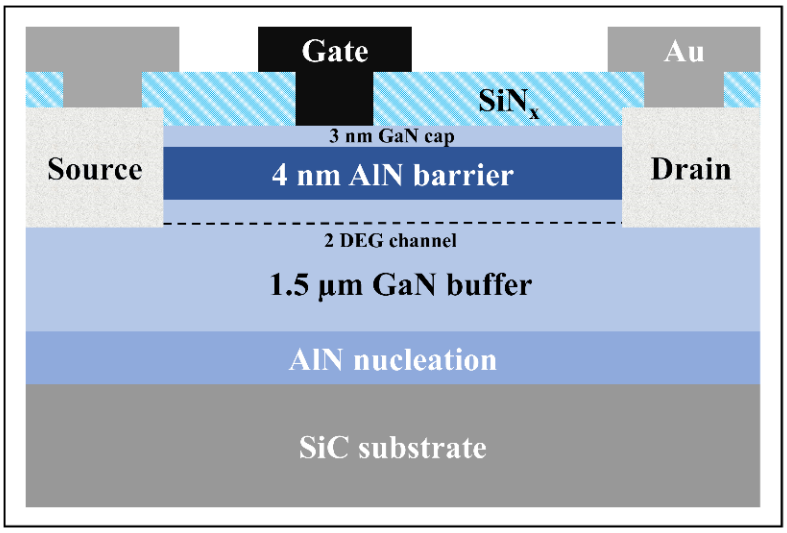

Figure 8. Structural illustration of AlN/GaN HEMT. Adapted from Ref. [111].

Comparing both the structures fabricated by MOCVD and MBE (as shown in Figure 8), differences in Al composition and Al distribution among the samples are observed. There is 100% Al content in the MBE sample but the MOCVD sample shows 50 to 60% Al content. The Al profile for both MBE and MOCVD samples is detected by Scanning Transmission Electron Microscopy–Energy Dispersive X-ray Spectroscopy (STEM-EDX) testing. The Al profile changed after annealing the MBE sample such that the sample became similar to that of the MOCVD sample. The drastic change in Al profile after annealing the MBE sample shows that the growth temperature highly influences the Al distribution [111]. The structural and electrical properties of MBE and MOCVD samples show different results. For the MBE sample, there is an increased sheet resistance and a decrease in mobility. Further, after SiN deposition and annealing, the surface chemistry is changed, and a decrease in surface potential is observed. A decrease in mobility is observed for the MBE sample, but no change is observed for the MOCVD sample. The MOCVD sample was a contact resistance of 0.3 Ωmm exhibited great achievements with a sheet carrier density of 1.1×10^{13} cm^{-2}, mobility of 1480 cm^2 $V^{-1}s^{-1}$, and an overall sheet resistance of 376 Ω sq^{-1}. Figure 9 shows the DC output and transfer characteristics of the HEMT. It is seen that the device can be operated up to 15 V, and a short channel effect is observed by flat output conductance. A very high transconductance is shown in Figure 9b of 600 mS/mm. The results shown in Figure 9a,b are of the MOCVD-based fabricated AlN/GaN HEMT [111].

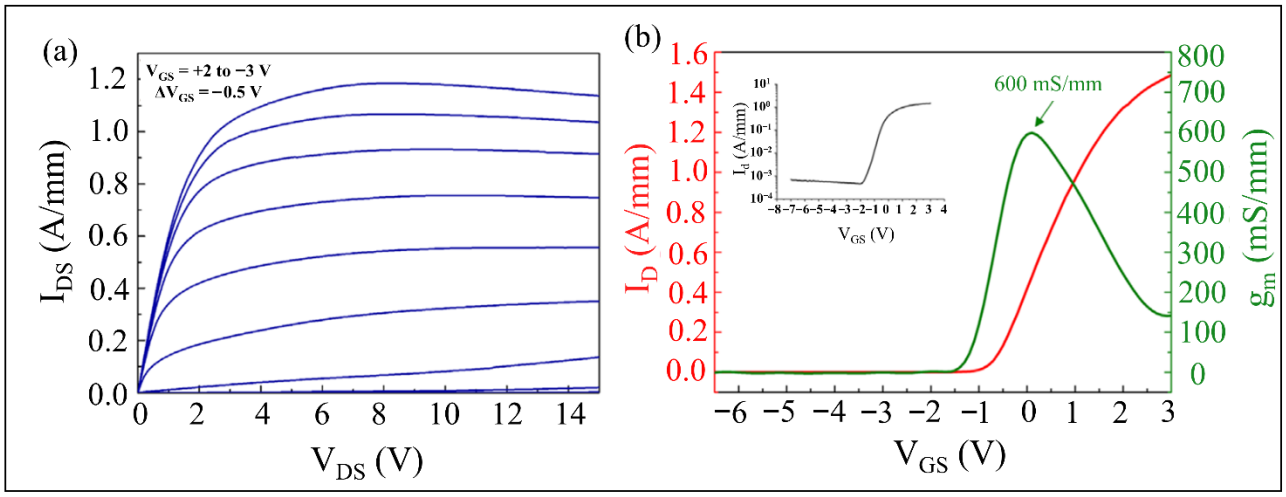

Figure 9. (**a**) Drain to source current versus voltage; (**b**) gate to source current and transconductance versus voltage curve. The inset highlights the measured gate and drain leakage currents. Reproduced with permission from Ref. [111].

The first study of HEMT investigated the fabrication process of AlGaN/GaN HEMTs and demonstrated that the quality and uniformity of the device layers have a strong impact on device performance. The step-by-step process has been described in detail, providing a comprehensive and systematic explanation of each fabrication stage. Another HEMT device is fabricated via MBE and MOCVD methods, named AlN/GaN HEMT. The comparison shows that high-quality layers have been formed by MOCVD, and the MBE structure degraded with time. Some of the advantages include a high-quality device and a commercially viable technique, which make MOCVD ideal. But if the precursor flow and temperature are not controlled properly, it can result in degradation of the device.

2.3. LEDs

LEDs produce light through electron–hole recombination, while conventional bulbs generate illumination by filament heating or gas discharge, whereas LEDs rely on electroluminescence. British scientist Henry Joseph Round discovered the concept of electroluminescence back in 1907, which led to the LED technology [112]. The first visible LED was fabricated by Nick Holonyak Jr., a scientist at the General Electric Company, in 1962 [113]. In the late twentieth century, different colored LEDs such as red, green, yellow, and orange, were introduced [114–117]. Shuji Nakamura, Hiroshi Amano, and Isamu Akasaki invented the blue GaN-based LED in 1993 and later received the Nobel Prize for this invention in 2014 [118]. Other prizes for the invention include the Global Energy Prize (2015), Queen Elizabeth Prize for Engineering (2021), and Kyoto Prize (2009). White LEDs, a key industry goal, have been produced by mixing red, blue, and green light [119–121]. LEDs have revolutionized everyday applications, including solid-state lighting, display technologies, and automotive lighting systems [122–131].

2.3.1. Challenges

Some challenges faced while fabricating III–V-based or quantum well LEDs are dislocation, lattice mismatch, controlling precursor gases, and controlling growth conditions. The main issue while growing GaN thin films is that there is lattice mismatch between GaN and substrates like Si and SiC. It can cause different defects and impurities within the device, which reduces the reliability and efficiency of an LED. Furthermore, the implication of the MOCVD technique during growth faces different challenges like reactor contamination, poor control of the precursor gases flow, material quality, etc. The control of precursor gases

during the doping of different layers is also important to optimize the device structure and enhance the optical and electronic properties of the device. Another significant challenge faced during the fabrication of GaN-based LEDs is the built-in electric field, which causes the confined stark effect. It results in a longer carrier lifetime, and the recombination rate is reduced, which results in poor performance. Further, different techniques like multi-junction, quantum well, and quantum dot structures have been introduced to decrease non-radiative recombination, obtain uniform current injection, and enhance the efficiency of LED. Overcoming these issues and challenges requires precise regulation over the growth process and conditions, resulting in better performance devices [17,132–134]. Despite these challenges, MOCVD supports complex heterostructure designs essential for high-efficiency LEDs, outpacing other growth methods in productivity while offering a more precise layer control than HVPE. These advantages outweigh its higher operating costs and safety demands, solidifying MOCVD as the industry standard for commercial optoelectronic device fabrication.

2.3.2. Epitaxial Growth of LEDs by MOCVD

MOCVD and MBE are the common techniques used for the fabrication of III–V optoelectronic devices. But MOCVD emerged as a prime candidate for commercial applications [135,136]. MOCVD is used to grow LEDs layer-by-layer on a GaAs substrate. Figure 10 shows the step-by-step fabrication process of the multi-quantum well (MQW)-based AlGaInP/GaInP micro-LED. Figure 10 shows the micro-LED structure based on the AlGaInP/GaInP MQW configuration. The first step of fabrication is to clean the substrate with acetone, methanol, and deionized water. The Inductively Coupled Plasma Reactive Ion Etching (ICP-RIE) technique is used to define the pixels and etch away the sides of AlGaInP/GaInP layers. In the ICP-RIE reactor, chlorine (Cl_2) and argon (Ar) gases are used, and the sidewalls of layers up to the n-InGaP layer are etched away. The n-doped InGaP epitaxial layer is selectively etched from the substrate using a 3:1 (v/v) phosphoric acid (H_3PO_4):hydrochloric acid (HCl) solution. Al_2O_3 is deposited to avoid the short circuit of p-contact. The buffered oxide etchant is used to remove the Al_2O_3 layer from one side of the device. The next step is to use an electron beam evaporator to deposit a (25/75) nm layer of Cr/Au on the Al_2O_3 layer. Then, a contact Pd/Ge/Au (20/40/100 nm) is deposited on the substrate layer. To minimize the resistance of ohmic contacts, annealing of the sample is done for 10 min at a temperature of 200 °C. Surface passivation with the (1:5) solution of HCl:DI water is utilized for oxide removal from the sidewalls. To minimize the formation of native oxide, the device is put into the atomic layer deposition (ALD) chamber. The last step is to deposit a 10 nm passivation layer of Al_2O_3 on the sample. The stepwise process of manufacturing AlGaInP/GaInP MQW LED is shown in Figure 10. Two samples with and without passivation are tested for different sizes ranging from 15×15 μm^2 to 80×80 μm^2. The surface passivated devices show superior performance [137].

Further, MOCVD with the Vapor Liquid Solid (VLS) and Vapor Solid (VS) techniques is used to grow a GaN-based nanowire LED. A metal alloy catalyst is used to initiate the growth process of the GaN nanowire core as shown in Figure 11a [138,139]. Next, the VS method is used to cover the nanowire with a GaN shell. The precursor is introduced into the chamber, which reacts with the nanowire surfaces and forms a shell, as shown in Figure 11b. Next, InGaN/GaN layers are grown over the shell surface, where InGaN acts as a quantum well layer and GaN acts as a quantum barrier layer, as shown in Figure 11c. Figure 11d shows the structure with a GaN nanowire (NW) encased by a GaN shell structure and an InGaN/GaN structure. Figure 11e,f show the glass substrate image after the deposition of gold (Au) and the growth of InGaN/GaN structure. Figure 11g shows the agglomeration of the Au/In/Ga alloy catalyst. The diameter of these nanoparticles

is 42 ± 10 nm. The amount of catalyst controlled the diameter of nanowires, shown by SEM image in Figure 11h. The amount and supply of gallium and nitrogen precursors can help control and optimize the GaN nanowire growth rate [140]. Utilizing a Au or Ni catalyst to grow GaN nanowires by the VLS technique results in better quality as compared to other traditional methods [141]. The active region InGaN/GaN structure is grown by the VS technique. This helps reduce the impurities caused by the catalyst, as no catalyst is used in the VS technique. The SEM image shown in Figure 11 represents the growth of the GaN shell on the nanowire structure. Figure 11g–l show the SEM image of InGaN/GaN structured nanowires grown on substrate. The SEM images clearly show that a uniform structure is grown on a glass substrate. The grown uniform structure shows that it is free from any impurities, and no deterioration is observed. This indicates that GaN nanowire can be used for large-scale applications [142].

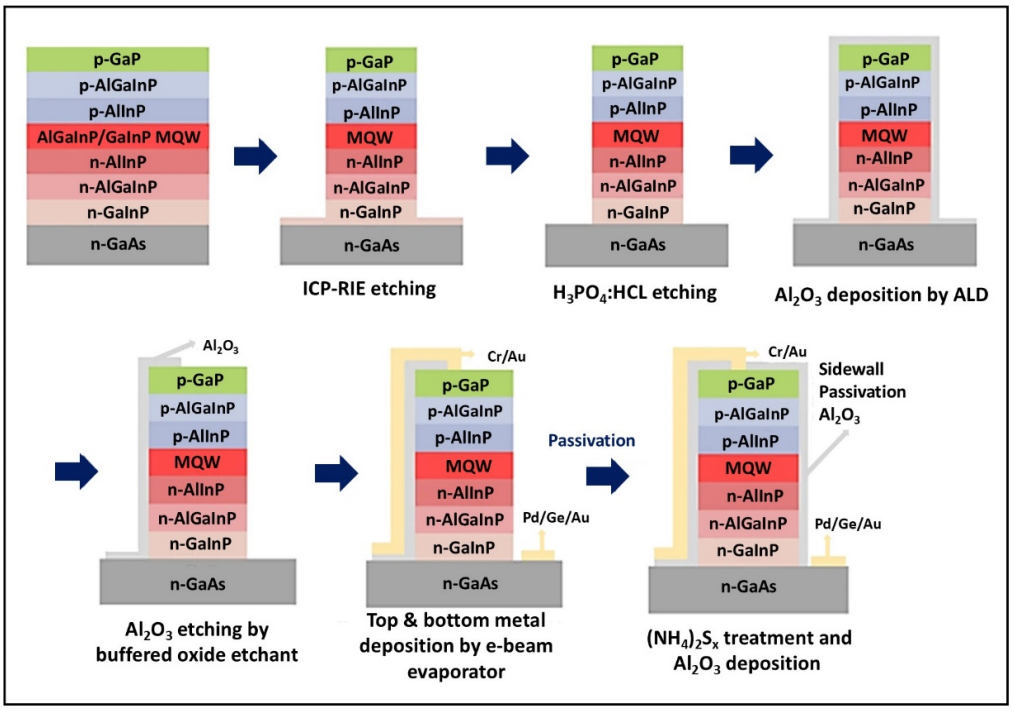

Figure 10. Step-by-step fabrication of AlGaInP/GaInP MQW LED via MOCVD. Reused under creative common license [137].

A new MOCVD reactor, designated G10-AsP and based on Planetary Reactor® technology [143], has been introduced. It incorporates a novel four-fold gas inlet system and chlorine-based in situ cleaning to enable growth on large-diameter InP substrates. The study reports the successful deposition of two key structures for telecommunication applications: (1) a highly strained AlGaInAs multiple quantum well (MQW) emitting at 1550 nm and (2) a 500 nm InGaAsP bulk layer emitting at 1100 nm, both grown on 150 mm wafers [144]. Fabrication and passivation in AlGaInP/GaInP micro-LED using MOCVD have been reported [137], demonstrating a 20% enhancement in external quantum efficiency (EQE) and an approximately 14% reduction in surface recombination velocity. A GaN nanowire LED is successfully fabricated on an amorphous glass substrate using MOCVD, achieving an internal quantum efficiency of 76.1%, as determined through temperature-dependent photoluminescence measurements [142]. Strain-compensated multi-quantum wells (SCMQWs) of InGaAs/GaAsP are grown by low-pressure (69.76 Torr) metal–organic chemical vapor deposition (LP-MOCVD) and employed as the active region of near-infrared light-emitting diodes [145]. LP-MOCVD improves quantum well growth by suppressing parasitic gas-

phase reactions, enhancing interface abruptness, and promoting smooth step-flow morphology, all of which strengthen radiative efficiency and structural integrity [146]. Thus, the optimized structure achieved an output optical power of approximately 10.5 mW and a quantum efficiency of 18% under a bias current of 50 mA, demonstrating the effectiveness of strain compensation in enhancing radiative recombination and reducing defect-related losses compared to conventional MQWs.

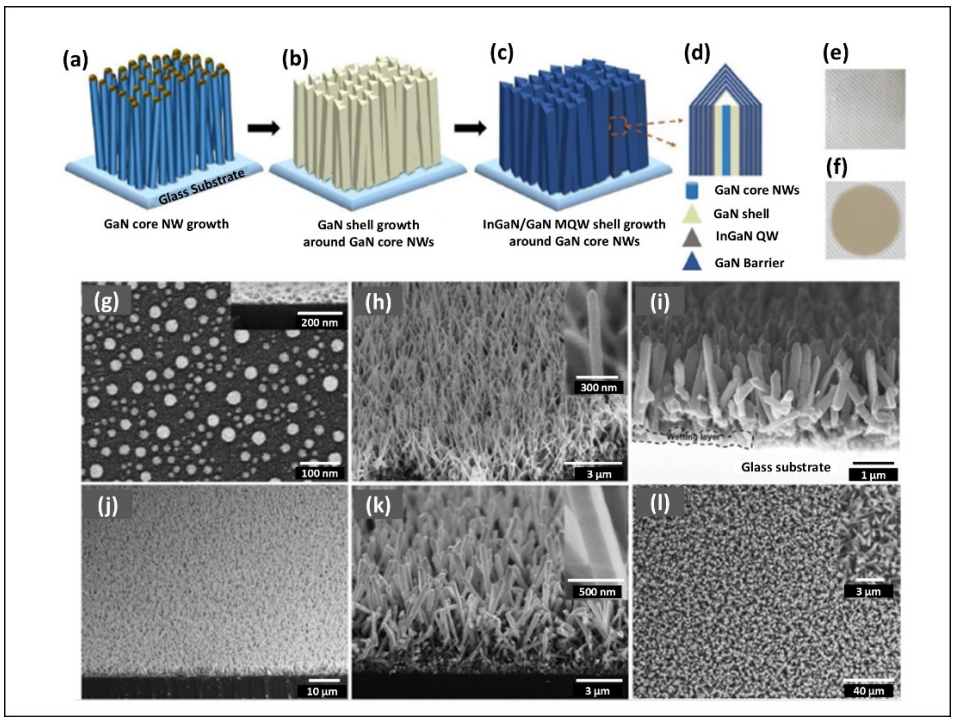

Figure 11. (**a**) Growth of GaN NW; (**b**) growth of GaN coating over GaN NW; (**c**) growth of InGaN/GaN MQW coating over GaN coating; (**d**) schematic view of the final structure; (**e**) deposition of Au on substrate; (**f**) growth of InGaN/GaN MQW; SEM images of (**g**) agglomeration of catalyst, (**h**) GaN NWs, (**i**) GaN coating growth over GaN NW; (**j**) view of final structure of InGaN/GaN MQW NWs; (**k**) high-resolution image of final structure; and (**l**) overhead view of final structure. Reproduced with permission from Ref. [142].

These studies underscore the advantages of MOCVD, such as precise control over layer thickness and composition, capability to fabricate nano- and micro-scale devices, and suitability for large-scale production. However, traditional challenges have included the use of toxic precursors, high equipment costs, difficulties in compositional control for complex multi-layer structures, and defect formation when growth parameters are not optimized. Recent technological advances, such as improved precursor delivery systems, in situ cleaning techniques, and real-time monitoring, have significantly mitigated these issues, thus, reducing impurity incorporation, enhancing uniformity, and improving process reproducibility. Consequently, MOCVD remains a highly adaptable and reliable technique for next-generation III–V semiconductor devices.

2.4. Laser Diodes

A laser diode, at its core, is a direct bandgap semiconductor p-n junction. The semiconductors used are typically III–V compounds like GaAs or InP, where carrier injection leads to population inversion in the active region. When electrons recombine with holes, spontaneous emission initiates photon generation. These photons then stimulate further emissions from excited carriers, producing a cascade of coherent photons. The structure incorporates optical feedback via cleaved facets or integrated mirrors, forming a Fabry–Pérot

or distributed feedback (DFB) cavity that supports mode selection and threshold gain for lasing. The laser diode is a p-n junction diode with a structure like LEDs except that there is a reflective mirror (and a waveguide) in the laser diode structure [147]. Unlike LEDs, which emit incoherent and omnidirectional light, laser diodes produce highly directional, monochromatic, and phase-coherent beams with significantly higher brightness and modulation speeds. These attributes make them indispensable in a wide array of applications including optical communication, consumer electronics, defense, medical, automotive, and scientific research [148–152]. The development of the laser diode dates to 1962, when Robert N. Hall and co-workers at General Electric reported the first semiconductor laser, which emitted coherent infrared radiation from a GaAs p–n junction [153]. In the same year, Nick Holonyak Jr., also at General Electric, demonstrated the first semiconductor laser diode operating in the visible red region using a gallium arsenide phosphide (GaAsP) alloy, thereby establishing the basis for modern visible LEDs and laser diodes [154]. In 1963, a group of scientists working under Nikolay Basov in the Soviet Union also demonstrated GaAs lasers [155,156].

2.4.1. Challenges

While MOCVD is the predominant technique for commercial laser diode production, achieving the requisite material quality presents distinct challenges. The foremost issue is the suppression of defects, particularly threading dislocations, which act as non-radiative recombination centers and elevate the lasing threshold, ultimately limiting device lifetime and efficiency. This is exacerbated when growing on low-cost, lattice-mismatched substrates like silicon. Precise control over interface abruptness in quantum well structures is another critical hurdle. Any interface roughness or elemental interdiffusion, often caused by thermal instability of precursors like trimethylindium, broadens the gain spectrum and degrades performance. Furthermore, the incorporation of certain elements, such as bismuth in GaAsBi or indium in InGaN, is highly sensitive to growth temperature and the V/III ratio, making reproducibility difficult and often leading to phase separation or droplet formation (as illustrated in Figure 12). Beyond technical growth issues, significant challenges relate to safety and cost. The use of highly toxic hydride precursors (e.g., arsine, phosphine) mandates rigorous safety protocols and infrastructure, thus, increasing the operational complexity and cost. Thus, for optimal performance, controlled utilization of precursors and reduction in defects is inevitable. The mass-scale production of large semiconductor (III–V) wafers is also a significant challenge considering control over the growth conditions, while maintaining compositional and thickness uniformity [157,158]. Despite this, MOCVD is the widely used growth method for LDs due to their high throughput, scalability for mass production, excellent control over alloy composition, doping for MQWs, distributed Bragg reflector (DBR) structures, cost-effectiveness, and uniformity.

2.4.2. Epitaxial Growth of Laser Diodes by MOCVD

MOCVD is used to grow $GaAs_{1-z}Bi_z$ laser diodes [159]. The incorporation of Bi into GaAs enables significant bandgap reduction (~60–90 meV per % Bi) while increasing the spin–orbit splitting energy. This allows for improved bandgap engineering for multi-junction solar cells, extended wavelength absorption, and potential suppression of Auger recombination losses [160,161]. To grow the desired laser diode, the precursors used are tri-isopropyl-gallium (TIPGa), trimethylbismuth (TMBi), tertiarybutylarsine (TBAs), and triethylgallium (TEGa). During the growth process, a temperature of 365 °C is used, and the $GaAs_{1-z}Bi_z$/GaAs quantum well structure of the laser diode is grown with GaAs substrate. To design this laser diode, a reactor AIX200-GFR system (AIXTRON) [7,162] is used with a pressure of 50 mbar (37.5 Torr). Hydrogen is used as a carrier gas. The structure is grown

at 375 °C and 400 °C. The growth rates of 0.88 mm/h and 0.41 mm/h are observed at 400 °C and 375 °C. GaAs and GaAsBi have the same growth rates, whereas the growth conditions are controlled to optimize the thickness of the device. The AFM image shows the morphological features of the samples. Figure 12a shows the even bismuth distribution across one sample. In Figure 12b, the flow of the Bi precursor is increased and Bi segregation is observed as drops in the sample. In Figure 12c, the flow of the Bi precursor is further increased and Bi segregation is observed in the form of larger drops in the sample. Samples shown in Figure 12a–c are grown at a temperature of 400 °C. The fourth sample shows the sample free of any Bi droplets, and it is grown at a temperature of 375 °C with Bi content of 4.2%, as illustrated in Figure 12d. Figure 12e shows a graph with Bi content on the y-axis and precursor ratio (TMBi/TBAs+ TMBi) on the x-axis. The temperatures of the growing samples are 375 °C and 400 °C. The ratio of TBAs and TEGa supply remained constant at 2.1. The graph shows that increasing the precursor's amount increases the Bi content. When the temperature is reduced from 400 °C to 375 °C, the Bi content is increased from 2.7% to 4.2%. Furthermore, it is observed that as the TMBi amount is increased, the Bi content is increased. After a certain limit, it becomes constant [159,163–166].

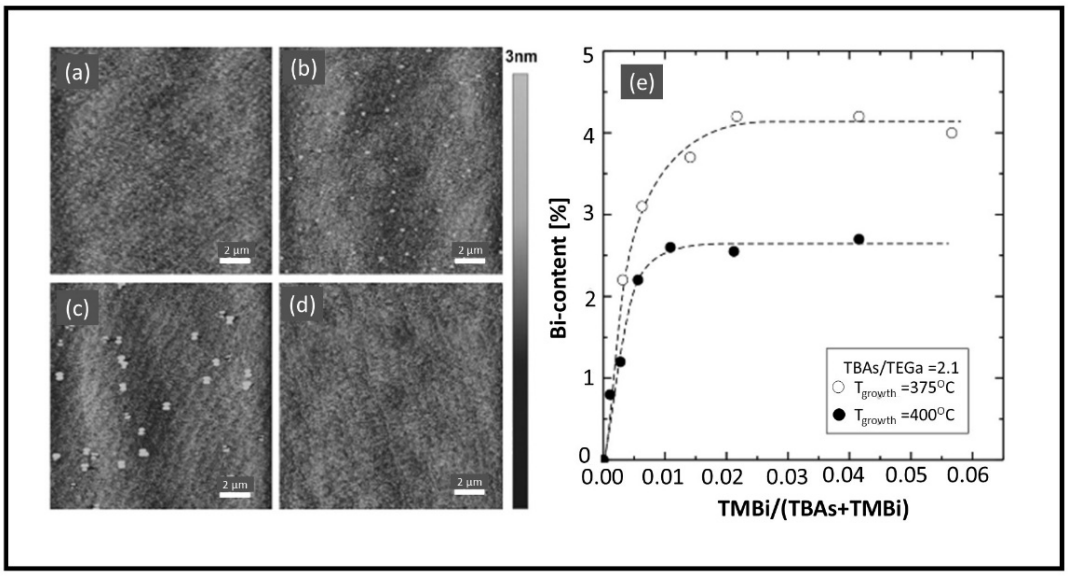

Figure 12. GaAsBi/GaAs MQW morphology with different growth conditions: (**a**–**c**) growth temperature of 400 °C and (**d**) growth temperature of 375 °C and 4.2% Bi concentration. The TMBi/V ratio for (**a**) 0.0056, (**b**) 0.021, and (**c**) 0.042. (**e**) Bi content versus TMBi/(TBAs+TMBi) at different growth temperatures of 375 °C and 400 °C. Reproduced with permission from Ref. [166].

Quantum dot laser diode structures can be grown via MOCVD. Figure 13a shows the device's structure. MOCVD is employed to grow a Ge-based buffer layer on a silicon substrate. In the Ge layer, the threading dislocation density utilized is $5 \times 10^6/cm^2$ and the substrate is doped with phosphorus. The Ge/Si virtual substrate is held at a temperature of 400 °C, and the oxide desorption process is carried out. The next step is to raise the temperature to 650 °C and maintain it for 20 min. The substrate is cooled down to 380 °C. The next step is to grow the GaAs layer by adopting the Ga pre-layer growth method [167,168]. Next, the AlGaAs-based cladding and guiding layer are grown with Al-content of 40% and 20%, respectively. Next, an InAs/InGaAs quantum dot laser structure with dot-in-well (DWELL) is grown under optimized conditions. Then, AlGaAs-based guiding and cladding layers are grown, with a thickness of 55 nm and 1.5 µm, respectively. The last GaAs contacting layer is grown, with a thickness of 300 nm. Light output power versus current (L-I) is tested for the pulsed and continuous wave (cw) modes.

The laser diode on different heatsink temperatures for the case of pulsed and cw modes are shown in Figure 13b,c. The laser diode operated with pulsed mode works up to 84 °C heatsink temperature. The maximum output power is for the case of 21 °C and has a value of 6.1 mW. For the continuous mode operated laser structure, 30 °C is the maximum temperature. The maximum output power for this case is 12 mW at a temperature of 12 °C. Room-temperature lasing is achieved at a wavelength of 1.28 µm for ridge-waveguide lasers with as-cleaved facets, exhibiting threshold current densities of 163 A/cm^2 under continuous wave operation and 64.3 A/cm^2 under pulsed operation [169].

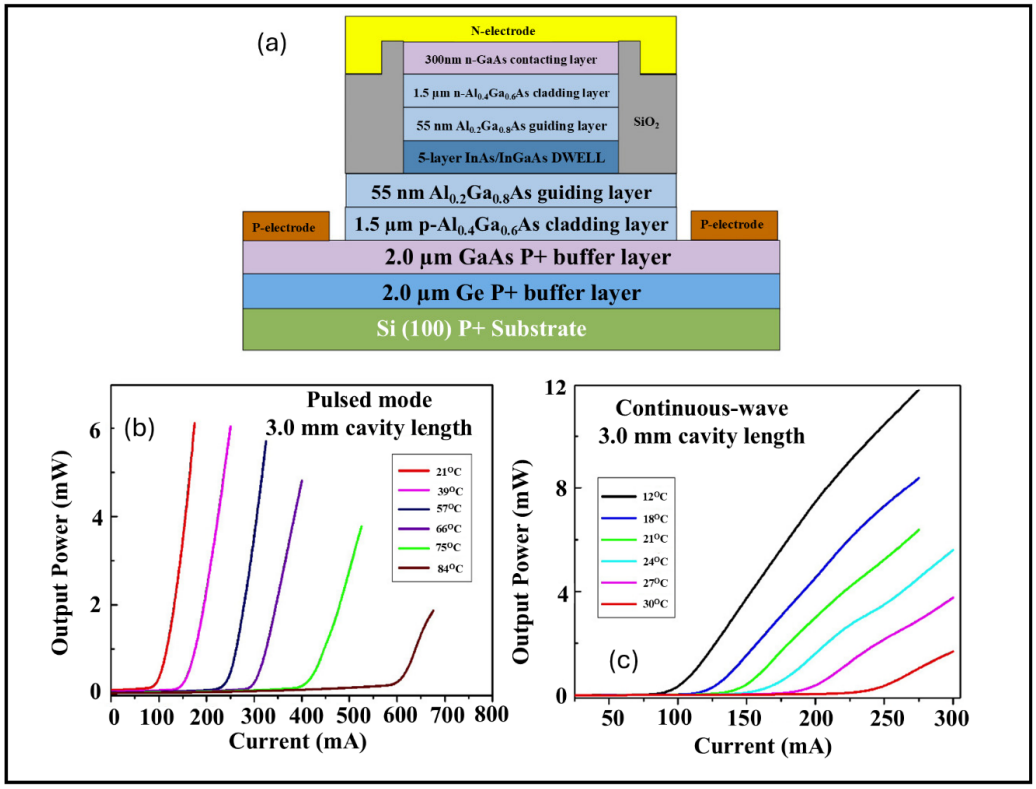

Figure 13. (**a**) Structure of InAs/GaAs QD laser diode; light output power versus current under the condition of (**b**) pulsed mode and (**c**) continuous wave. Reused under creative common license [169].

The successful growth of Ga(AsBi)/GaAs multi-quantum well structure via MOCVD shows that control over Bi content is required here to achieve the desired bandgap engineering for each layer of the device. The next study reported the growth of InAs/GaAs quantum dot laser diodes, attaining remarkably low threshold current densities, which highlights the capability of MOCVD as a growth technique. It highlights the advantages of MOCVD, which comprises control over composition, thickness uniformity, interface sharpness, and feasibility in fabricating quantum dots and well structures. However, some of the disadvantages are the sensitive nature of this technique towards temperature and precursor, and the high risk while handling toxic precursors. Still, these studies reaffirm that MOCVD remains one of the most reliable and versatile techniques for fabricating advanced structures.

2.5. Photonic Integrated Circuits

Photonic integrated circuits (PICs) represent a transformative technology for next-generation systems, enabling unprecedented scalability and performance in optical communication, sensing, and computing. By integrating optical and electronic components on a single chip, PICs deliver high-speed data processing and ultra-broadband connectivity es-

sential for applications such as 6G networks, quantum information systems, and AI-driven architectures [170–174]. Unlike traditional electronic circuits, PICs manipulate photons instead of electrons, drastically reducing resistive losses and heat generation. This photon-based approach minimizes power consumption because optical signals propagate without the need for continuous charge transport, eliminating Joule heating and allowing energy-efficient modulation and routing. A key enabler of PIC performance is the use of III–V semiconductor materials such as indium phosphide (InP) and gallium arsenide (GaAs), which offer direct bandgap properties essential for efficient light generation, amplification, and modulation. These materials allow for monolithic integration of lasers, modulators, and detectors on-chip, making PICs indispensable for state-of-the-art applications such as data centers, edge computing, and emerging photonic technologies.

2.5.1. Challenges

MOCVD growth of PICs encounters several critical challenges that influence both device performance and large-scale manufacturability. Growing high-quality, free of defects structures with precise control over thickness and composition is necessary but also challenging. The main challenge is the lattice mismatch between different layers, which can cause strain, dislocation, and imperfections in the structure. Maintaining uniformity across large wafers is also challenging, as the variation in temperature or flow of precursor can cause non-uniformity in thickness and composition. It can also impact the generation, amplification, and magnification of photon signals within the device, eventually making it unsuitable for device operation. Excellent control over doping profiles and nanometer precision of interfaces is crucial for devices like lasers and photodetectors, but variations in these growth factors can increase optical loss and reduce the efficiency of the device. The incorporation of heterogeneous material systems, such as wide-bandgap semiconductors integrated on silicon platforms, adds further complexity related to thermal stability and chemical compatibility. Moreover, achieving consistent reproducibility and scalability for commercial manufacturing—while simultaneously optimizing growth rates and suppressing defect formation—continues to be a major challenge in MOCVD-based PIC fabrication [4,175].

2.5.2. Epitaxial Growth of Photonic Integrated Circuits by MOCVD

An InP-based quantum cascade laser (QCL), which operates in the long-wavelength infrared region (λ = 9 μm), is fabricated via MOCVD [176]. The etching of the double channels is done, and a semi-insulating InP: Fe is filled to enhance the heat dissipation. For insulation, a 450 nm thick SiO_2 layer is deposited via the CVD technique, and an electrical contact made of a Ti/Au layer is deposited by electron beam evaporation. Another gold layer is deposited to improve heat dissipation, and a metal contact layer made of Ge/Au/Ni/Au is deposited on the substrate. Then, the waveguides are cleaved, and back and front facets are introduced. The surface of the front facet is not coated with anything, and the back facet is coated with ZrO_2/Ti/Au/Ti/Al_2O_3 and is highly reflective. Next, photolithography and wet chemical etching have been used to fabricate the double-channel ridge structure. The device has a ridge structure, which shows anisotropy and reduces electrical loss. To improve the performance, a diamond heatsink with indium is present, and the device is attached to the epitaxial side of that structure. This structure is further soldered to the copper sink. The thermopile detector is used to measure the output power of the device, and the collection efficiency is nearly 100%. It shows a 1.55 W of maximum pulsed peak power and a 1.02 W of continuous wave peak power at 293 K. A very low 1.52 kA/cm^2 pulsed threshold current density of the device is measured. The electroluminescence spectrum exhibited a full width at a half maximum (FWHM) of

466 cm^{-1}. The measured characteristic temperature coefficients are 228 K for the threshold current and 680 K for the slope efficiency. The general working mechanism and structure of a quantum cascade laser (QCL) is shown in Figure 14. Some of the applications of the QCLs are gas sensing and environmental monitoring, free space optical communication, medical diagnostics, spectroscopy, imaging, and sensing [10,177–184].

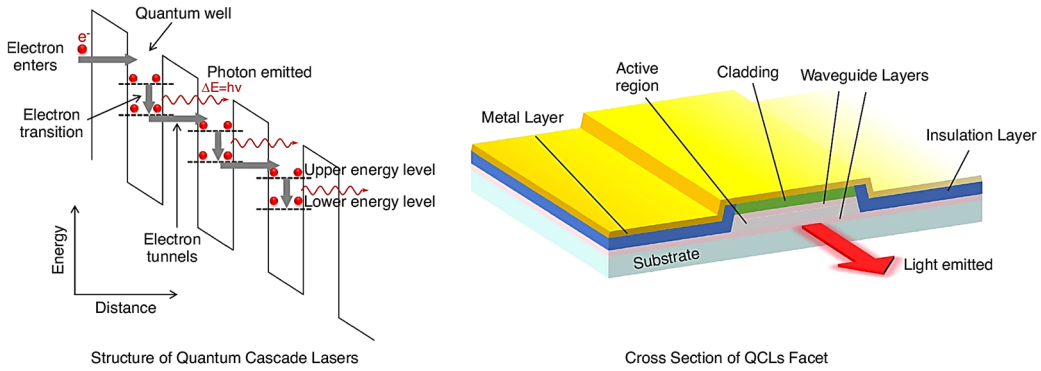

Figure 14. Working principle of quantum cascade laser and its geometry structure. Reused under creative common license [185].

The MOCVD method is used to fabricate Ga_2O_3 films on a Si/SiO_2 template. It uses pure oxygen, TMGA, and pure argon as the precursor gases. Before the growth of films, the template is sequentially cleaned by ultrasonic treatment in acetone, anhydrous ethanol, and deionized water for 5 min each, followed by drying with nitrogen gas. The chamber pressure during growth is set at 40 kPa (300 Torr). Additionally, 7 mL/min and 400 mL/min are the flow rates of TMGa and pure oxygen, respectively. The effect of temperature on Ga_2O_3 thin films is tested, and it is found that an increase in growth temperature results in the transition of films from an amorphous state to a polycrystalline state. The growth temperature is optimized to get amorphous films. Further, some simulations have been done to design the structure of the waveguide. Here, Ga_2O_3, SiO_2, and air are set as the core, substrate, and cladding layer, respectively. The next step is to fabricate the waveguide via MOCVD, which is simulated before. Ga_2O_3 amorphous films with 310 nm thickness are grown, and a Si/SiO_2 template is used with the MOCVD method. Then, UV lithography and RIE are used as patterning for these films. The etching gases used here are BCl_3 and Ar. Moreover, 300W and 200W RIE power and bias power are set here, respectively. The etching pressure and BCl_3/Ar flow rate used here are 1 Pa and 20/5 sccm, respectively. Further, different tests are conducted to investigate the characteristics of the waveguide structure. The truncation method is used here to analyze optical loss. At 1550 nm, the optical loss of the Ga_2O_3 waveguide is 12.4 dB/cm. It is demonstrated that the amorphous state of Ga_2O_3 films fabricated via the MOCVD method is best suited for use in waveguide applications. Figure 15a depicts the surface morphology of the Ga_2O_3 film grown on a Si/SiO_2 template at 510 °C, as observed by SEM. The SEM image showed that the structure's layers are uniform and exhibit smooth, precisely defined interfaces. Owing to the low growth temperature, no obvious crystalline phases are detected in the Ga_2O_3 film. This suggests that the film exhibits an amorphous structure, in agreement with the XRD analysis. Furthermore, the EDX elemental mappings of Si, O, and Ga are presented in Figure 15b–d. The homogeneous distribution of oxygen and gallium across the film indicates negligible interfacial segregation. As shown in Figure 15e, the High-Resolution Transmission Electron Microscopy (HRTEM) image verifies the amorphous nature of the Ga_2O_3 and SiO_2 layers. These results indicate that the employed deposition methods effectively produced homogeneous, amorphous Ga_2O_3 thin films with clean and stable

interfaces, which are essential for the fabrication of optical waveguides requiring precise control of material properties and interfacial quality [186].

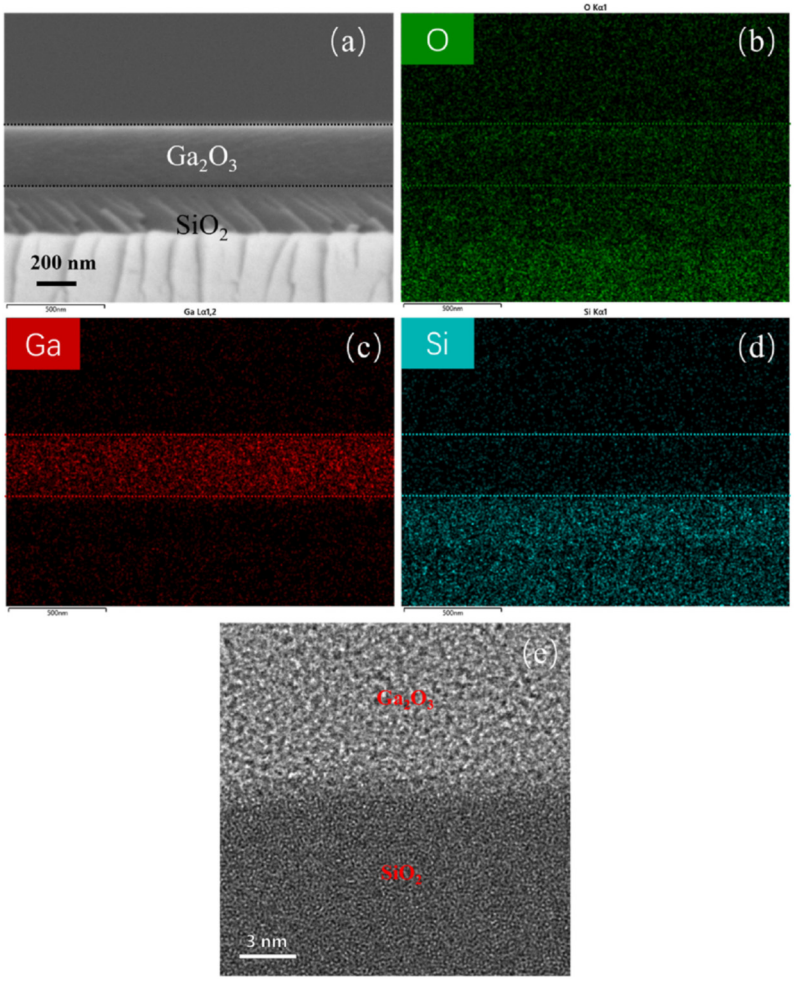

Figure 15. (**a**) The cross-sectional SEM and EDX mapping of (**b**) O, (**c**) Ga, and (**d**) Si and the cross-sectional HRTEM of (**e**) the Ga_2O_3/Si bilayer structure grown at a temperature of 510 °C. Reproduced with permission from Ref. [186].

3. Conclusions and Future Directions

This review explores the history, applications, and challenges of MOCVD in growing next-generation state-of-the-art III–V semiconductor devices. MOCVD allows for unparalleled control over semiconductor film thickness, uniform growth, composition, and dopant concentrations, and has propelled tremendous technological advancements from LEDs and laser diodes to high-electron-mobility transistors. These controls are critical in improving the output characteristics of next-generation semiconductor devices. On top of this, the scalability of MOCVD has led to its commercial deployment at industrial scales, beyond the lab. One key area of interest is the development of low-temperature growth processes using MOCVD, which will eventually help in fabricating polymers and organic-based flexible substrates [187,188]. MOCVD operates at >600 °C, while most flexible substrates (PET, PEN) degrade above 200 °C. Some emerging approaches such as plasma-assisted MOCVD ($\leq$150 °C) for oxides like Al_2O_3 can be deployed. In high-performance optoelectronics, achieving atomic-scale control over composition, doping, and interface abruptness in complex heterostructures remains a bottleneck [189,190]. For quantum photonics and advanced heterostructures, lattice mismatch and defect density in III–V/Si and III–V/2D integrations are being addressed through strain-compensated buffer layers, selective-area

growth, and patterned substrate engineering. In power electronics, scaling MOCVD for wide-bandgap materials such as GaN, AlN, and Ga_2O_3 demands large-wafer uniformity and defect reduction [191–193]. Advanced reactor hydrodynamics, computational fluid dynamics (CFD)-guided flow optimization, and novel precursor delivery systems are to be explored. Furthermore, the integration of state-of-the-art in situ monitoring technologies (e.g., spectroscopic ellipsometry, RHEED, mass spectrometry) is expected to effectively upgrade the film formation process and reduce the cost using MOCVD. AI-driven processes, digital twins, precursor recycling, and energy-efficient reactor designs are emerging as solutions to improve yield, shorten development cycles, reduce environmental impact, and cut costs by minimizing trial runs. Challenges remain in model training but, with ever-evolving advanced models, these innovations promise faster development cycles and lower production costs for advanced optoelectronics [194,195].

The integration of GaN with two-dimensional (2D) materials offers a transformative approach for next-generation photodetectors, yet several challenges remain [196]. Future research should prioritize interface engineering to achieve defect-free GaN/2D heterojunctions and minimize trap states, alongside band alignment control through gate-tunable and strain-engineered architectures for dynamic spectral modulation. Advancing device designs, such as vertical heterostructures and multi-layer 2D stacks, can enhance light absorption and carrier separation, while incorporating plasmonic elements may enable ultra-fast detection. Performance optimization will require strategies to improve responsivity and detectivity in self-powered mode, reduce dark current, and ensure low-noise operation. Beyond conventional applications, GaN/2D systems offer opportunities for bio-inspired multispectral imaging, polarization-sensitive detection, and flexible photodetectors for wearable electronics. Reliability studies under harsh conditions—such as radiation, high temperature, and mechanical stress—are essential for aerospace and defense deployment. Finally, scalable fabrication methods, including MOCVD-grown GaN layers combined with wafer-scale 2D material transfer, and integration into CMOS-compatible platforms will be critical for commercial viability and widespread adoption in intelligent edge devices.

The trajectory of MOCVD research and industrial deployment over the next few years will be shaped by the convergence of materials innovation, process intelligence, and application-driven engineering. In flexible and wearable electronics, the maturation of low-temperature plasma-assisted MOCVD and hybrid MOCVD–ALD processes are expected to unlock this exciting area [197–199]. The fusion of MOCVD with heterogeneous integration platforms combining III–V semiconductors with silicon photonics, 2D materials, and organic electronics will open entirely new market verticals, from autonomous sensing to space-qualified systems and implantable biomedical devices. As these advances converge, MOCVD is poised to transition from a specialized epitaxy method to a universally adaptable manufacturing platform, underpinning the next generation of optoelectronic, quantum, and energy-efficient devices at both industrial and consumer scales [200–202].

Author Contributions: Conceptualization, M.U.; methodology, Z.N., M.U., S.A., A.N. and A.H.; software, Z.N., M.U. and S.A.; validation, Z.N. and M.U.; formal analysis, Z.N., M.U. and S.A.; investigation, Z.N., M.U. and S.A.; resources, Z.N., M.U. and S.A.; data curation, Z.N., M.U. and S.A.; writing—original draft preparation, Z.N.; writing—review and editing, Z.N., M.U. and S.A.; supervision, M.U. and A.A.; project administration, M.U. and A.A.; funding acquisition, A.A. All authors have read and agreed to the published version of the manuscript.

Funding: The research received no external funding.

Data Availability Statement: The data that support the findings of this study are available from the corresponding author upon reasonable request.

Acknowledgments: The authors are obliged to Ghulam Ishaq Khan Institute of Engineering Sciences and Technology (Pakistan) for providing the needed resources for this research.

Conflicts of Interest: The authors declare that they have no known competing financial interests or personal relationships that could have appeared to influence the work reported in this paper.

References

1. Bohr, M.T.; Young, I.A. CMOS scaling trends and beyond. *IEEE Micro* **2017**, *37*, 20–29. [CrossRef]
2. Lundstrom, M.S.; Alam, M.A. Moore's law: The journey ahead. *Science* **2022**, *378*, 722–723. [CrossRef]
3. Bohlemann, C.Y.; Flötotto, A.; Paszuk, A.; Nandy, M.; Großmann, M.; Romanyuk, O.; Hanke, K.D.; Gieß, A.; Kleinschmidt, P.; Runge, E. Surface structure of MOVPE-prepared As-modified Si (100) substrates. *Appl. Surf. Sci.* **2024**, *675*, 160879. [CrossRef]
4. Davies, J.I.; Johnson, A.D.; Pelzel, R.I.; Geen, M.D.; Joel, A.M.; Lim, S.W. MOVPE and its future production challenges. *J. Cryst. Growth* **2023**, *605*, 127031. [CrossRef]
5. Saxena, P.; Srivastava, P.; Srivastava, A. MOCVD/MOVPE epitaxy of group III–V nitride with atomistic Prospective & cost Effectiveness. *J. Cryst. Growth* **2025**, *650*, 127975.
6. Maury, F. Recent trends in the selection of metal-organic precursors for MOCVD process. *J. Phys. IV* **1995**, *5*, C5-449–C5-463. [CrossRef]
7. Juergensen, H. MOCVD technology in research, development and mass production. *Mater. Sci. Semicond. Process.* **2001**, *4*, 467–474. [CrossRef]
8. Fujii, T.; Hiraki, T.; Aihara, T.; Nishi, H.; Takeda, K.; Sato, T.; Kakitsuka, T.; Tsuchizawa, T.; Matsuo, S. Development of an epitaxial growth technique using iii–v on a si platform for heterogeneous integration of membrane photonic devices on si. *Appl. Sci.* **2021**, *11*, 1801. [CrossRef]
9. Grützmacher, D.; Concepción, O.; Zhao, Q.-T.; Buca, D. Si–Ge–Sn alloys grown by chemical vapour deposition: A versatile material for photonics, electronics, and thermoelectrics. *Appl. Phys. A* **2023**, *129*, 235. [CrossRef]
10. Zhou, X.; Zhai, L.; Liu, J. Epitaxial quantum dots: A semiconductor launchpad for photonic quantum technologies. *Photonics Insights* **2023**, *1*, R07. [CrossRef]
11. Kotamraju, S.; Sukeerthi, M.; Puthanveettil, S.E. Modeling of InGaP/InGaAs-GaAsP/Ge multiple quantum well solar cell to improve efficiency for space applications. *Sol. Energy* **2019**, *186*, 328–334. [CrossRef]
12. Shieh, H.M.; Fu, R.J.; Lu, T.-C.; Chen, L.-R. High-performance GaInP/AlGaInP visible laser diodes grown by multiwafer MOCVD. In *Laser Diodes and LEDs in Industrial, Measurement, Imaging, and Sensors Applications II; Testing, Packaging, and Reliability of Semiconductor Lasers V*; SPIE: Bremerhaven, Germany, 2000; pp. 214–219.
13. White, R.C.; Kim, B.; Wang, Y.; Dhingra, P.; Lee, M.L. InP quantum dot lasers: From growth to devices. *Opt. Mater. Express* **2025**, *16*, 32–54. [CrossRef]
14. Wu, Y.; Liu, B.; Xu, F.; Sang, Y.; Tao, T.; Xie, Z.; Wang, K.; Xiu, X.; Chen, P.; Chen, D. High-efficiency green micro-LEDs with GaN tunnel junctions grown hybrid by PA-MBE and MOCVD. *Photonics Res.* **2021**, *9*, 1683–1688. [CrossRef]
15. Liu, Z.J.; Huang, T.; Ma, J.; Liu, C.; Lau, K.M. Monolithic integration of AlGaN/GaN HEMT on LED by MOCVD. *IEEE Electron Device Lett.* **2014**, *35*, 330–332. [CrossRef]
16. Coleman, J.; Lammert, R.; Osowski, M.; Jones, A. Progress in InGaAs-GaAs selective-area MOCVD toward photonic integrated circuits. *IEEE J. Sel. Top. Quantum Electron.* **2002**, *3*, 874–884. [CrossRef]
17. Tan, A.; Hamzah, N.; Ahmad, M.; Ng, S.; Hassan, Z. Recent advances and challenges in the MOCVD growth of indium gallium nitride: A brief review. *Mater. Sci. Semicond. Process.* **2022**, *143*, 106545. [CrossRef]
18. Seshan, K. *Handbook of Thin Film Deposition*; William Andrew: Norwich, NY, USA, 2012.
19. Hidayat, W.; Usman, M. Applications of molecular beam epitaxy in optoelectronic devices: An overview. *Phys. Scr.* **2024**, *99*, 112002. [CrossRef]
20. Tsao, J.Y. *Materials Fundamentals of Molecular Beam Epitaxy*; Academic Press: Cambridge, MA, USA, 2012.
21. Sengupta, S.; Aggarwal, R.; Raula, M. A review on chemical bath deposition of metal chalcogenide thin films for heterojunction solar cells. *J. Mater. Res.* **2023**, *38*, 142–153. [CrossRef]
22. Gupta, B.; Hossain, M.A.; Riaz, A.; Sharma, A.; Zhang, D.; Tan, H.H.; Jagadish, C.; Catchpole, K.; Hoex, B.; Karuturi, S. Recent advances in materials design using atomic layer deposition for energy applications. *Adv. Funct. Mater.* **2022**, *32*, 2109105. [CrossRef]
23. Simon, A.H. Sputter processing. In *Handbook of Thin Film Deposition*; Elsevier: Amsterdam, The Netherlands, 2025; pp. 93–140.
24. Du, P.; Wang, L.; Li, J.; Luo, J.; Ma, Y.; Tang, J.; Zhai, T. Thermal evaporation for halide perovskite optoelectronics: Fundamentals, progress, and outlook. *Adv. Opt. Mater.* **2022**, *10*, 2101770. [CrossRef]
25. Thompson, A.G. MOCVD technology for semiconductors. *Mater. Lett.* **1997**, *30*, 255–263. [CrossRef]

26. Thompson, A.; Stall, R.; Kroll, W.; Armour, E.; Beckham, C.; Zawadzki, P.; Aina, L.; Siepel, K. Large scale manufacturing of compound semiconductors by MOVPE. *J. Cryst. Growth* **1997**, *170*, 92–96. [CrossRef]
27. Dupuis, R.D. III–V semiconductor quantum-well devices grown by metalorganic chemical vapor deposition. *Proc. IEEE* **2013**, *101*, 2188–2199. [CrossRef]
28. Stringfellow, G.B. *Organometallic Vapor-Phase Epitaxy: Theory and Practice*; Elsevier: Amsterdam, The Netherlands, 1999.
29. Ludowise, M. Metalorganic chemical vapor deposition of III–V semiconductors. *J. Appl. Phys.* **1985**, *58*, R31–R55. [CrossRef]
30. Wright, P.; Crosbie, M.; Lane, P.; Williams, D.; Jones, A.; Leedham, T.; Davies, H. Metal organic chemical vapor deposition (MOCVD) of oxides and ferroelectric materials. *J. Mater. Sci. Mater. Electron.* **2002**, *13*, 671–678. [CrossRef]
31. Khanna, V.K. *Fundamentals of Solid-State Lighting: LEDs, OLEDs, and Their Applications in Illumination and Displays*; CRC Press: Boca Raton, FL, USA, 2014.
32. Kuech, T. Metal-organic vapor phase epitaxy of compound semiconductors. *Mater. Sci. Rep.* **1987**, *2*, 1–49. [CrossRef]
33. Grodzinski, P.; DenBaars, S.P.; Lee, H. From research to manufacture—The evolution of MOCVD. *JOM* **1995**, *47*, 25–32. [CrossRef]
34. Manasevit, H.; Simpson, W.I. The use of metal-organics in the preparation of semiconductor materials: I. Epitaxial gallium-V compounds. *J. Electrochem. Soc.* **1969**, *116*, 1725. [CrossRef]
35. Manasevit, H. The use of metalorganics in the preparation of semiconductor materials: Growth on insulating substrates. *J. Cryst. Growth* **1972**, *13*, 306–314. [CrossRef]
36. Acher, O.; Koch, S.; Omnes, F.; Defour, M.; Drévillon, B.; Razeghi, M. In Situ Investigation of the Low Pressure MOCVD Growth of Lattice-Mismatched Semiconductors using Reflectance Anisotropy Measurements. In *Condensed Systems of Low Dimensionality*; Springer: Berlin/Heidelberg, Germany, 1991; pp. 409–433.
37. Zhao, H. Low Pressure Chemical Vapor Deposition. In *Gallium Oxide: Materials Properties, Crystal Growth, and Devices*; Higashiwaki, M., Fujita, S., Eds.; Springer International Publishing: Cham, Switzerland, 2020; pp. 293–306.
38. Mullin, J.; Irvine, S.; Tunnicliffe, J. MOVPE of narrow gap II–VI compounds. *J. Cryst. Growth* **1984**, *68*, 214–222. [CrossRef]
39. Kawai, H.; Kaneko, K.; Watanabe, N. Photoluminescence of AlGaAs/GaAs quantum wells grown by metalorganic chemical vapor deposition. *J. Appl. Phys.* **1984**, *56*, 463–467. [CrossRef]
40. Dupuis, R.; Dapkus, P.; Kolbas, R.; Holonyak, N. Quantum-well $Al_xGa_{1-x}As$-GaAs heterostructure lasers grown by metalorganic chemical vapor deposition. *IEEE J. Quantum Electron.* **2003**, *15*, 756–761. [CrossRef]
41. Holonyak, N., Jr.; Kolbas, R.; Dupuis, R.; Dapkus, P. Room-temperature continuous operation of photopumped MO-CVD $Al_xGa_{1-x}As$-GaAs-$Al_xGa_{1-x}As$ quantum-well lasers. *Appl. Phys. Lett.* **1978**, *33*, 73–75. [CrossRef]
42. Fotiadis, D.I.; Kieda, S.; Jensen, K.F. Transport phenomena in vertical reactors for metalorganic vapor phase epitaxy: I. Effects of heat transfer characteristics, reactor geometry, and operating conditions. *J. Cryst. Growth* **1990**, *102*, 441–470. [CrossRef]
43. Nakada, T.; Mizutani, M. 18% efficiency Cd-free Cu (In, Ga) Se_2 thin-film solar cells fabricated using chemical bath deposition (CBD)-ZnS buffer layers. *Jpn. J. Appl. Phys.* **2002**, *41*, L165. [CrossRef]
44. Barrioz, V.; Irvine, S.; Jones, E.; Rowlands, R.; Lamb, D. In situ deposition of cadmium chloride films using MOCVD for CdTe solar cells. *Thin Solid Film.* **2007**, *515*, 5808–5813. [CrossRef]
45. Carta, G.; Natali, M.; Rossetto, G.; Zanella, P.; Salmaso, G.; Restello, S.; Rigato, V.; Kaciulis, S.; Mezzi, A. A comparative study of Cr_2O_3 thin films obtained by MOCVD using three different precursors. *Chem. Vap. Depos.* **2005**, *11*, 375–380. [CrossRef]
46. Biethan, J.-P.; Sirkeli, V.; Considine, L.; Nedeoglo, D.; Pavlidis, D.; Hartnagel, H.L. Photoluminescence study of ZnO nanostructures grown on silicon by MOCVD. *Mater. Sci. Eng. B* **2012**, *177*, 594–599. [CrossRef]
47. Kang, T.-T.; Liu, X.; Zhang, R.Q.; Hu, W.G.; Cong, G.; Zhao, F.-A.; Zhu, Q. InN nanoflowers grown by metal organic chemical vapor deposition. *Appl. Phys. Lett.* **2006**, *89*, 071113. [CrossRef]
48. Milanov, A.P.; Fischer, R.A.; Devi, A. Synthesis, characterization, and thermal properties of homoleptic rare-earth guanidinates: Promising precursors for MOCVD and ALD of rare-earth oxide thin films. *Inorg. Chem.* **2008**, *47*, 11405–11416. [CrossRef]
49. Tuna, Ö.; Behmenburg, H.; Giesen, C.; Kalisch, H.; Jansen, R.; Yablonskii, G.; Heuken, M. Dependence of InN properties on MOCVD growth parameters. *Phys. Status Solidi C* **2011**, *8*, 2044–2046. [CrossRef]
50. Yang, C.; Wang, X.; Xiao, H.; Zhang, X.; Hu, G.; Ran, J.; Wang, C.; Li, J.; Li, J.; Wang, Z. Growth temperature dependences of InN films grown by MOCVD. *Appl. Surf. Sci.* **2008**, *255*, 3149–3152. [CrossRef]
51. Nam, S.H.; Hyun, J.-S.; Boo, J.-H. Synthesis of TiO_2 thin films using single molecular precursors by MOCVD method for dye-sensitized solar cells application and study on film growth mechanism. *Mater. Res. Bull.* **2012**, *47*, 2717–2721. [CrossRef]
52. Norris, K.J.; Lohn, A.J.; Onishi, T.; Coleman, E.; Wong, V.; Shakouri, A.; Tompa, G.S.; Kobayashi, N.P. MOCVD growth of erbium monoantimonide thin film and nanocomposites for thermoelectrics. *J. Electron. Mater.* **2012**, *41*, 971–976. [CrossRef]
53. Sang, L.; Liao, M.; Sumiya, M. A comprehensive review of semiconductor ultraviolet photodetectors: From thin film to one-dimensional nanostructures. *Sensors* **2013**, *13*, 10482–10518. [CrossRef] [PubMed]
54. Gawron, W.; Sobieski, J.; Manyk, T.; Kopytko, M.; Madejczyk, P.; Rutkowski, J. MOCVD grown HgCdTe heterostructures for medium wave infrared detectors. *Coatings* **2021**, *11*, 611. [CrossRef]

55. Lundin, W.; Talalaev, R. Epitaxial Systems for III–V and III-Nitride MOVPE. In *Metalorganic Vapor Phase Epitaxy (MOVPE) Growth, Materials Properties, and Applications*; Wiley Semiconductors: Hoboken, NJ, USA, 2019; pp. 423–466.
56. Liu, H.; Wang, Q.; Chen, J.; Liu, K.; Ren, X. MOCVD growth and characterization of multi-stacked InAs/GaAs quantum dots on misoriented Si (100) emitting near 1.3 μm. *J. Cryst. Growth* **2016**, *455*, 168–171. [CrossRef]
57. Mrowiński, P.; Musiał, A.; Gawarecki, K.; Dusanowski, Ł.; Heuser, T.; Srocka, N.; Quandt, D.; Strittmatter, A.; Rodt, S.; Reitzenstein, S. Excitonic complexes in MOCVD-grown InGaAs/GaAs quantum dots emitting at telecom wavelengths. *Phys. Rev. B* **2019**, *100*, 115310. [CrossRef]
58. Siriwongrungson, V.; Alkaisi, M.M.; Krumdieck, S.P. Step coverage of thin titania films on patterned silicon substrate by pulsed-pressure MOCVD. *Surf. Coat. Technol.* **2007**, *201*, 8944–8949. [CrossRef]
59. Thompson, J.; Mackett, P.; Jenkin, G.; Duy, T.N.; Gori, P. The growth of CdHgTe by metalorganic chemical vapour deposition for optical communication devices. *J. Cryst. Growth* **1988**, *86*, 917–923. [CrossRef]
60. Schygulla, P.; Müller, R.; Lackner, D.; Höhn, O.; Hauser, H.; Bläsi, B.; Predan, F.; Benick, J.; Hermle, M.; Glunz, S.W.; et al. Two-terminal III–V//Si triple-junction solar cell with power conversion efficiency of 35.9% at AM1.5g. *Prog. Photovolt. Res. Appl.* **2022**, *30*, 869–879. [CrossRef]
61. Lo Presti, F.; Pellegrino, A.L.; Malandrino, G. Metal-organic chemical vapor deposition of oxide perovskite films: A facile route to complex functional systems. *Adv. Mater. Interfaces* **2022**, *9*, 2102501. [CrossRef]
62. Yu, D.S.; Meng, L.; Zhao, H. MOCVD growth of β-Ga_2O_3 with fast growth rates (>4.3 μm/h), low controllable doping, and superior transport properties. *Appl. Phys. Lett.* **2024**, *125*, 242106. [CrossRef]
63. Chen, C.-Y.; Zhu, G.; Hu, Y.; Yu, J.-W.; Song, J.; Cheng, K.-Y.; Peng, L.-H.; Chou, L.-J.; Wang, Z.L. Gallium Nitride Nanowire Based Nanogenerators and Light-Emitting Diodes. *ACS Nano* **2012**, *6*, 5687–5692. [CrossRef] [PubMed]
64. Holzwarth, J.; Miccoli, I.; Boyd, A.; Korst, T.; Heuken, M. Advancements in MOCVD technology for low cost high quality epitaxy. In *Light-Emitting Devices, Materials, and Applications XXVIII*; SPIE: Bremerhaven, Germany, 2024; pp. 24–27.
65. Petrova-Koch, V. Milestones of solar conversion and photovoltaics. In *High-Efficient Low-Cost Photovoltaics: Recent Developments*; Springer: Berlin/Heidelberg, Germany, 2009; pp. 1–5.
66. Hersch, P.; Zweibel, K. *Basic Photovoltaic Principles and Methods*; Solar Energy Research Institute (SERI): Golden, CO, USA, 1982.
67. Dutta, A.K. Prospects of nanotechnology for high-efficiency solar cells. In Proceedings of the 2012 7th International Conference on Electrical and Computer Engineering, Dhaka, Bangladesh, 20–22 December 2012; pp. 347–350.
68. Andreani, L.C.; Bozzola, A.; Kowalczewski, P.; Liscidini, M.; Redorici, L. Silicon solar cells: Toward the efficiency limits. *Adv. Phys. X* **2019**, *4*, 1548305. [CrossRef]
69. Schindler, F.; Michl, B.; Krenckel, P.; Riepe, S.; Benick, J.; Mueller, R.; Richter, A.; Glunz, S.W.; Schubert, M.C. Optimized multicrystalline silicon for solar cells enabling conversion efficiencies of 22%. *Sol. Energy Mater. Sol. Cells* **2017**, *171*, 180–186. [CrossRef]
70. Metzger, W.K.; Grover, S.; Lu, D.; Colegrove, E.; Moseley, J.; Perkins, C.; Li, X.; Mallick, R.; Zhang, W.; Malik, R. Exceeding 20% efficiency with in situ group V doping in polycrystalline CdTe solar cells. *Nat. Energy* **2019**, *4*, 837–845. [CrossRef]
71. Takamoto, T.; Ikeda, E.; Kurita, H.; Ohmori, M.; Yamaguchi, M.; Yang, M.-J. Two-terminal monolithic $In_{0.5}Ga_{0.5}P$/GaAs tandem solar cells with a high conversion efficiency of over 30%. *Jpn. J. Appl. Phys.* **1997**, *36*, 6215. [CrossRef]
72. Machín, A.; Márquez, F. Advancements in Photovoltaic Cell Materials: Silicon, Organic, and Perovskite Solar Cells. *Materials* **2024**, *17*, 1165. [CrossRef]
73. Geisz, J.F.; Steiner, M.A.; Garcia, I.; Kurtz, S.R.; Friedman, D.J. Enhanced external radiative efficiency for 20.8% efficient single-junction GaInP solar cells. *Appl. Phys. Lett.* **2013**, *103*, 041118. [CrossRef]
74. Green, M.A. *Third Generation Photovoltaics: Advanced Solar Energy Conversion*; Springer: Berlin/Heidelberg, Germany, 2006.
75. Jain, N.; Schulte, K.L.; Geisz, J.F.; France, R.M.; Steiner, M.A. GaInAsP/GaInAs tandem solar cell with 32.6% one-sun efficiency. In Proceedings of the 2017 IEEE 44th Photovoltaic Specialist Conference (PVSC), Washington, DC, USA, 25–30 June 2017; pp. 232–235.
76. Steiner, M.; Geisz, J.; García, I.; Friedman, D.; Duda, A.; Kurtz, S. Optical enhancement of the open-circuit voltage in high quality GaAs solar cells. *J. Appl. Phys.* **2013**, *113*, 123109. [CrossRef]
77. Rahman, M.U.; Usman, M.; Sayyad, M.H.; Abbas, S.Z. Impact of carbon electrode layer on the series resistance and fill factor of CH3NH3PbI3 perovskite solar cell. *Phys. Scr.* **2024**, *99*, 105974. [CrossRef]
78. Noor, Z.; Usman, M.; Islam, M.J.; Bashir, J.; Shakir, S.W.; Naveed, A. Intrinsic layer-enhanced InGaP/GaAs solar cell: A path to higher efficiency. *J. Renew. Sustain. Energy* **2025**, *17*, 033701. [CrossRef]
79. Baiju, A.; Yarema, M. Status and challenges of multi-junction solar cell technology. *Front. Energy Res.* **2022**, *10*, 971918. [CrossRef]
80. Dey, S.K.; Alluri, P.V. PE-MOCVD of dielectric thin films: Challenges and opportunities. *MRS Bull.* **1996**, *21*, 44–48. [CrossRef]
81. Jain, N.; Hudait, M.K. III–V multijunction solar cell integration with silicon: Present status, challenges and future outlook. *Energy Harvest. Syst.* **2014**, *1*, 121–145. [CrossRef]

82. Kim, Y.; Kim, K.; Lee, J.; Kim, C.Z.; Kang, H.K.; Park, W.-K. Epitaxial Ge solar cells directly grown on Si (001) by MOCVD using isobutylgermane. *J. Korean Phys. Soc.* **2018**, *72*, 633–638. [CrossRef]
83. Kim, Y.; Kim, K.; Kim, C.Z.; Jung, S.H.; Kang, H.K.; Park, W.-K.; Lee, J. Highly efficient epitaxial Ge solar cells grown on GaAs (001) substrates by MOCVD using isobutylgermane. *Sol. Energy Mater. Sol. Cells* **2017**, *166*, 127–131. [CrossRef]
84. Grassman, T.J.; Chmielewski, D.J.; Carnevale, S.D.; Carlin, J.A.; Ringel, S.A. $GaAs_{0.75}P_{0.25}$/Si dual-junction solar cells grown by MBE and MOCVD. *IEEE J. Photovolt.* **2015**, *6*, 326–331. [CrossRef]
85. Stolt, L.; Hedström, J.; Kessler, J.; Ruckh, M.; Velthaus, K.O.; Schock, H.W. ZnO/CdS/$CuInSe_2$ thin-film solar cells with improved performance. *Appl. Phys. Lett.* **1993**, *62*, 597–599. [CrossRef]
86. Fan, P.; Liang, G.-X.; Zheng, Z.-H.; Cai, X.-M.; Zhang, D.-P. Growth and characterization of CIS thin films prepared by ion beam sputtering deposition. *Chin. Phys. Lett.* **2010**, *27*, 046801. [CrossRef]
87. Huang, H.-C.; Lin, C.-S.; Chang, W.-C. Electrodeposition of CIS films on the Mo back electrodes with different crystallinities. *Electrochim. Acta* **2012**, *75*, 20–27. [CrossRef]
88. Irvine, S.; Barrioz, V.; Lamb, D.; Jones, E.; Rowlands-Jones, R. MOCVD of thin film photovoltaic solar cells—Next-generation production technology? *J. Cryst. Growth* **2008**, *310*, 5198–5203. [CrossRef]
89. Choi, I.-H. The preparation of a $CuInSe_2$ solar cell by metal organic chemical vapor deposition. *Thin Solid Film.* **2012**, *525*, 137–140. [CrossRef]
90. Lee, S.H.; Lee, G.H.; Lee, H.-S.; Kim, D.; Kang, Y. Characterization of mocvd-prepared cis solar cells. *Energies* **2021**, *14*, 7721. [CrossRef]
91. Nag, B. High electron mobility transistor (HEMT). *Phys. Quantum Well Devices* **2000**, 173–187. [CrossRef]
92. Hidayat, W.; Usman, M.; Shakir, S.W.; Ali, S. Dual-gate AlGaN channel HEMTs: Advancements in E-mode performance with N-shaped graded composite barriers. *Electron. Struct.* **2024**, *6*, 045001. [CrossRef]
93. Hidayat, W.; Usman, M. Breaking the limits of HEMT performance: InGaN channel and back barrier engineering. *Phys. B Condens. Matter* **2025**, *705*, 417069. [CrossRef]
94. Lee, C.; Sheng, N.; Lewis, H.; Wang, H.; Miller, D.; Donovan, J. GaAs/GaAlAs high electron mobility transistors for analog-to-digital converter applications. In Proceedings of the 1985 International Electron Devices Meeting, Washington, DC, USA, 1–4 December 1985; pp. 324–327.
95. Mimura, T. The early history of the high electron mobility transistor (HEMT). *IEEE Trans. Microw. Theory Tech.* **2002**, *50*, 780–782. [CrossRef]
96. Vandamme, E.; Schreurs, D.; Van Dinther, G. Electron Devices. *IEEE Trans.* **1994**, *48*, 737–742. [CrossRef]
97. Aadit, M.N.A.; Kirtania, S.G.; Afrin, F.; Alam, M.K.; Khosru, Q.D.M. High electron mobility transistors: Performance analysis, research trend and applications. In *Different Types of Field-Effect Transistors-Theory and Applications*; BoD: Hamburg, Germany, 2017; pp. 45–64.
98. Aucoin, L., IV. HEMTs and PHEMTs. In *GaAs MMIC Reliability Assurance Guideline forSpace Applications*; NASA: Washington, DC, USA, 1996; p. 39.
99. Lee, Y.-J.; Yao, Y.-C.; Huang, C.-Y.; Lin, T.-Y.; Cheng, L.-L.; Liu, C.-Y.; Wang, M.-T.; Hwang, J.-M. High breakdown voltage in AlGaN/GaN HEMTs using AlGaN/GaN/AlGaN quantum-well electron-blocking layers. *Nanoscale Res. Lett.* **2014**, *9*, 433. [CrossRef]
100. Wu, Y.-F.; Kapolnek, D.; Ibbetson, J.P.; Parikh, P.; Keller, B.P.; Mishra, U.K. Very-high power density algan/gan hemts. *IEEE Trans. Electron Devices* **2001**, *48*, 586–590.
101. Selvaraj, S.L.; Ito, T.; Terada, Y.; Egawa, T. AlN/ AlGaN/ GaN metal-insulator-semiconductor high-electron-mobility transistor on 4in. Silicon substrate for high breakdown characteristics. *Appl. Phys. Lett.* **2007**, *90*, 173506. [CrossRef]
102. Ramadan, A.; Martin, A.; Reveyrand, T.; Nebus, J.-M.; Bouysse, P.; Lapierre, L.; Villemazet, J.; Forestier, S. Efficiency enhancement of GaN power HEMTs by controlling gate-source voltage waveform shape. In Proceedings of the 2009 European Microwave Conference (EuMC), Rome, Italy, 29 September–1 October 2009; pp. 1840–1843.
103. Kucharski, R.; Sochacki, T.; Lucznik, B.; Bockowski, M. Growth of bulk GaN crystals. *J. Appl. Phys.* **2020**, *128*, 050902. [CrossRef]
104. Sakurai, H.; Omori, M.; Yamada, S.; Furukawa, Y.; Suzuki, H.; Narita, T.; Kataoka, K.; Horita, M.; Bockowski, M.; Suda, J. Highly effective activation of Mg-implanted p-type GaN by ultra-high-pressure annealing. *Appl. Phys. Lett.* **2019**, *115*, 142104. [CrossRef]
105. Islam, N.; Mohamed, M.F.P.; Khan, M.F.A.J.; Falina, S.; Kawarada, H.; Syamsul, M. Reliability, applications and challenges of GaN HEMT technology for modern power devices: A review. *Crystals* **2022**, *12*, 1581. [CrossRef]
106. Mizutani, T.; Ohno, Y.; Akita, M.; Kishimoto, S.; Maezawa, K. Current collapse in AlGaN/GaN HEMTs investigated by electrical and optical characterizations. *Phys. Status Solidi A* **2002**, *194*, 447–451. [CrossRef]
107. Islam, Z.; Paoletta, A.L.; Monterrosa, A.M.; Schuler, J.D.; Rupert, T.J.; Hattar, K.; Glavin, N.; Haque, A. Heavy ion irradiation effects on GaN/AlGaN high electron mobility transistor failure at off-state. *Microelectron. Reliab.* **2019**, *102*, 113493. [CrossRef]
108. Sangwan, V.; Tan, C.M.; Kapoor, D.; Chiu, H.-C. Electromagnetic induced failure in GaN-HEMT high-frequency power amplifier. *IEEE Trans. Ind. Electron.* **2019**, *67*, 5708–5716. [CrossRef]

109. Whiting, P.G.; Rudawski, N.G.; Holzworth, M.; Pearton, S.J.; Jones, K.S.; Liu, L.; Kang, T.; Ren, F. Nanocrack formation in AlGaN/GaN high electron mobility transistors utilizing Ti/Al/Ni/Au ohmic contacts. *Microelectron. Reliab.* **2017**, *70*, 41–48. [CrossRef]
110. Dubey, S.K.; Mishra, M.; Islam, A. Characterization of AlGaN/GaN based HEMT for low noise and high frequency application. *Int. J. Numer. Model. Electron. Netw. Devices Fields* **2022**, *35*, e2932. [CrossRef]
111. Godejohann, B.J.; Ture, E.; Müller, S.; Prescher, M.; Kirste, L.; Aidam, R.; Polyakov, V.; Brückner, P.; Breuer, S.; Köhler, K. AlN/GaN HEMTs grown by MBE and MOCVD: Impact of Al distribution. *Phys. Status Solidi B* **2017**, *254*, 1600715. [CrossRef]
112. Round, H.J. Light-emitting diodes hit the centenary milestone. *Electr. World* **1907**, *19*, 309–310.
113. Holonyak, N. Semiconductor alloy lasers–1962. *IEEE J. Quantum Electron.* **2003**, *23*, 684–691. [CrossRef]
114. Li, Y.; Hirosaki, N.; Xie, R.; Takeda, T.; Mitomo, M. Yellow-orange-emitting $CaAlSiN_3$: Ce^{3+} phosphor: Structure, photoluminescence, and application in white LEDs. *Chem. Mater.* **2008**, *20*, 6704–6714. [CrossRef]
115. Peter, M.; Laubsch, A.; Bergbauer, W.; Meyer, T.; Sabathil, M.; Baur, J.; Hahn, B. New developments in green LEDs. *Phys. Status Solidi A* **2009**, *206*, 1125–1129. [CrossRef]
116. Yorio, N.C.; Goins, G.D.; Kagie, H.R.; Wheeler, R.M.; Sager, J.C. Improving spinach, radish, and lettuce growth under red light-emitting diodes (LEDs) with blue light supplementation. *HortScience* **2001**, *36*, 380–383. [CrossRef]
117. Zhuang, Z.; Iida, D.; Ohkawa, K. InGaN-based red light-emitting diodes: From traditional to micro-LEDs. *Jpn. J. Appl. Phys.* **2021**, *61*, SA0809. [CrossRef]
118. Akasaki, I.; Amano, H.; Nakamura, S. Blue LEDs–Filling the world with new light. In *The Nobel Prize in Physics 2014*; Royal Swedish Academy of Sciences: Stockholm, Sweden, 2014.
119. Narukawa, Y.; Narita, J.; Sakamoto, T.; Yamada, T.; Narimatsu, H.; Sano, M.; Mukai, T. Recent progress of high efficiency white LEDs. *Phys. Status Solidi A* **2007**, *204*, 2087–2093. [CrossRef]
120. Sun, B.; Jiang, X.; Yung, K.-C.; Fan, J.; Pecht, M.G. A review of prognostic techniques for high-power white LEDs. *IEEE Trans. Power Electron.* **2016**, *32*, 6338–6362. [CrossRef]
121. Cho, J.; Park, J.H.; Kim, J.K.; Schubert, E.F. White light-emitting diodes: History, progress, and future. *Laser Photonics Rev.* **2017**, *11*, 1600147. [CrossRef]
122. Hadis, M.A.; Cooper, P.R.; Milward, M.R.; Gorecki, P.C.; Tarte, E.; Churm, J.; Palin, W.M. Development and application of LED arrays for use in phototherapy research. *J. Biophotonics* **2017**, *10*, 1514–1525. [CrossRef]
123. Tsao, J.Y.; Wierer, J.J.; Rohwer, L.E.; Coltrin, M.E.; Crawford, M.H.; Simmons, J.A.; Hung, P.-C.; Saunders, H.; Sizov, D.S.; Bhat, R. Ultra-efficient solid-state lighting: Likely characteristics, economic benefits, technological approaches. In *III-Nitride Based Light Emitting Diodes and Applications*; Springer: Singapore, 2017; pp. 11–28.
124. Mottier, P. *LED for Lighting Applications*; John Wiley & Sons: Hoboken, NJ, USA, 2010; Volume 134.
125. Pelka, D.G.; Patel, K. An overview of LED applications for general illumination. *Des. Effic. Illum. Syst.* **2003**, *5186*, 15–26.
126. Steranka, F.; Bhat, J.; Collins, D.; Cook, L.; Craford, M.; Fletcher, R.; Gardner, N.; Grillot, P.; Goetz, W.; Keuper, M. High power LEDs–Technology status and market applications. *Phys. Status Solidi A* **2002**, *194*, 380–388. [CrossRef]
127. Usman, M.; Malik, S.; Munsif, M. AlGaN-based ultraviolet light-emitting diodes: Challenges and opportunities. *Luminescence* **2021**, *36*, 294–305. [CrossRef]
128. Islam, N.U.; Usman, M.; Rasheed, S.; Jamil, T. White light-emitting diodes: Past, present, and future. *ECS J. Solid State Sci. Technol.* **2021**, *10*, 106004. [CrossRef]
129. Anwar, A.R.; Sajjad, M.T.; Johar, M.A.; Hernández-Gutiérrez, C.A.; Usman, M.; Łepkowski, S. Recent progress in micro-LED-based display technologies. *Laser Photonics Rev.* **2022**, *16*, 2100427. [CrossRef]
130. Esteki, M.; Khajehoddin, S.A.; Safaee, A.; Li, Y. LED systems applications and LED driver topologies: A review. *IEEE Access* **2023**, *11*, 38324–38358. [CrossRef]
131. Ali, S.; Usman, M. Dimensional downscaling and quantum engineering: A path to high-performance micro-LEDs. *J. Lumin.* **2025**, *277*, 120951. [CrossRef]
132. Fenwick, W. Progress and challenges in GaN-on-Si LEDs. *Light Emit. Diodes Mater. Devices Appl. Solid State Light. XX* **2016**, *9768*, 79–85.
133. Schumacher, M.; Lindner, J.; Baumann, P.; Schienle, F.; Solayappan, N.; Joshi, V.; Araujo, C.; McMillan, L. MOCVD for complex multicomponent thin films—A leading edge technology for next generation devices. *Mater. Sci. Semicond. Process.* **2002**, *5*, 85–91. [CrossRef]
134. Yu, B.; Li, Y.; Li, J.; Ding, X.; Li, Z. Challenges of high-yield manufacture in micro-light-emitting diodes displays: Chip fabrication, mass transfer, and detection. *J. Phys. D Appl. Phys.* **2024**, *57*, 463001. [CrossRef]
135. Nakamura, S.; Mukai, T.; Senoh, M. Candela-class high-brightness InGaN/AlGaN double-heterostructure blue-light-emitting diodes. *Appl. Phys. Lett.* **1994**, *64*, 1687–1689. [CrossRef]
136. Nakamura, S.; Senoh, M.S.M.; Mukai, T.M.T. P-GaN/N-InGaN/N-GaN double-heterostructure blue-light-emitting diodes. *Jpn. J. Appl. Phys.* **1993**, *32*, L8. [CrossRef]

137. Park, J.; Baek, W.; Geum, D.-M.; Kim, S. Understanding the sidewall passivation effects in AlGaInP/GaInP micro-LED. *Nanoscale Res. Lett.* **2022**, *17*, 29. [CrossRef] [PubMed]
138. Johar, M.A.; Waseem, A.; Hassan, M.A.; Kang, J.-H.; Ha, J.-S.; Lee, J.K.; Ryu, S.-W. Facile growth of high aspect ratio c-axis GaN nanowires and their application as flexible pn NiO/GaN piezoelectric nanogenerators. *Acta Mater.* **2018**, *161*, 237–245. [CrossRef]
139. Waseem, A.; Johar, M.A.; Hassan, M.A.; Bagal, I.V.; Ha, J.-S.; Lee, J.K.; Ryu, S.-W. Effect of crystal orientation of GaN/V_2O_5 core-shell nanowires on piezoelectric nanogenerators. *Nano Energy* **2019**, *60*, 413–423. [CrossRef]
140. Wu, S.; Wang, L.; Yi, X.; Liu, Z.; Yan, J.; Yuan, G.; Wei, T.; Wang, J.; Li, J. Crystallographic orientation control and optical properties of GaN nanowires. *RSC Adv.* **2018**, *8*, 2181–2187. [CrossRef] [PubMed]
141. Purushothaman, V.; Venkatesh, P.S.; Navamathavan, R.; Jeganathan, K. Direct comparison on the structural and optical properties of metal-catalytic and self-catalytic assisted gallium nitride (GaN) nanowires by chemical vapor deposition. *RSC Adv.* **2014**, *4*, 45100–45108. [CrossRef]
142. Johar, M.A.; Song, H.-G.; Waseem, A.; Hassan, M.A.; Bagal, I.V.; Cho, Y.-H.; Ryu, S.-W. Universal and scalable route to fabricate GaN nanowire-based LED on amorphous substrate by MOCVD. *Appl. Mater. Today* **2020**, *19*, 100541. [CrossRef]
143. Yang, F. Modern metal-organic chemical vapor deposition (MOCVD) reactors and growing nitride-based materials. In *Nitride Semiconductor Light-Emitting Diodes (LEDs)*; Elsevier: Amsterdam, The Netherlands, 2014; pp. 27–65.
144. Miccoli, I.; Simkus, G.; Larhirb, H.; Korst, T.; Mukinovic, M.; Holzwarth, J.; Heuken, M. Enabling MOCVD production on next generation 150 mm Indium Phosphide wafer size. *J. Cryst. Growth* **2024**, *643*, 127793. [CrossRef]
145. Yu, Y.; Qin, X.; Huang, B.; Wei, J.; Zhou, H.; Pan, J.; Chen, W.; Qi, Y.; Zhang, X.; Ren, Z. MOCVD growth of strain-compensated multi-quantum wells light emitting diode. *Vacuum* **2003**, *69*, 489–493. [CrossRef]
146. Razeghi, M. LP-MOCVD growth, characterization, and application of InP material. In *Semiconductors and Semimetals*; Elsevier: Amsterdam, The Netherlands, 1990; Volume 31, pp. 243–355.
147. Diehl, R.D. *High-Power Diode Lasers: Fundamentals, Technology, Applications*; Springer Science & Business Media: Berlin/Heidelberg, Germany, 2000; Volume 78.
148. Shakir, S.W.; Usman, M.; Habib, U.; Ali, S.; Mustafa, L. High-Power and High-Efficiency 221 nm AlGaN Far Ultraviolet Laser Diodes. *ECS J. Solid State Sci. Technol.* **2024**, *13*, 076001. [CrossRef]
149. Saeed, S.; Usman, M.; Aamir, M.; Islam, S. Graded Cladding Layers in Infrared III-Arsenide Separate Confinement Heterostructure Laser Diodes. *ECS J. Solid State Sci. Technol.* **2023**, *12*, 057009. [CrossRef]
150. Pinkerton, A.J. Lasers in additive manufacturing. *Opt. Laser Technol.* **2016**, *78*, 25–32. [CrossRef]
151. Kleine, K.F.; Whitney, B.; Watkins, K.G. Use of fiber lasers for micro cutting applications in the medical device industry. In *ICALEO 2002: 21st International Congress on Laser Materials Processing and Laser Microfabrication*; Laser Institute of America: Orlando, FL, USA, 2002.
152. Müller, G.J.; Berlien, P.; Scholz, C. The medical laser. *Med. Laser Appl.* **2006**, *21*, 99–108. [CrossRef]
153. Hall, R.N.; Fenner, G.E.; Kingsley, J.; Soltys, T.; Carlson, R. Coherent light emission from GaAs junctions. *Phys. Rev. Lett.* **1962**, *9*, 366. [CrossRef]
154. Holonyak, N., Jr.; Bevacqua, S.F. Coherent (visible) light emission from Ga (As_{1-x} P_x) junctions. In *Semiconductor Devices: Pioneering Papers*; World Scientific: Singapore, 1991; pp. 898–899.
155. Hecht, J. Short history of laser development. *Opt. Eng.* **2010**, *49*, 091002. [CrossRef]
156. Welch, D.F. A brief history of high-power semiconductor lasers. *IEEE J. Sel. Top. Quantum Electron.* **2000**, *6*, 1470–1477. [CrossRef]
157. Jung, H.; Ahn, N.; Klimov, V.I. Prospects and challenges of colloidal quantum dot laser diodes. *Nat. Photonics* **2021**, *15*, 643–655. [CrossRef]
158. Sciamanna, M.; Shore, K.A. Physics and applications of laser diode chaos. *Nat. Photonics* **2015**, *9*, 151–162. [CrossRef]
159. Mawst, L.J.; Kim, H.; Smith, G.; Sun, W.; Tansu, N. Strained-layer quantum well materials grown by MOCVD for diode laser application. *Prog. Quantum Electron.* **2021**, *75*, 100303. [CrossRef]
160. Liu, Y. Characterisation of GaAsBi Based Semiconductors. Ph.D. Thesis, The University of Sheffield, Sheffield, UK, 2020.
161. Maspero, R.; Sweeney, S.; Florescu, M. Unfolding the band structure of GaAsBi. *J. Phys. Condens. Matter* **2017**, *29*, 075001. [CrossRef]
162. Christiansen, K.; Luenenbuerger, M.; Schineller, B.; Heuken, M.; Juergensen, H. Advances in MOCVD technology for research, development and mass production of compound semiconductor devices. *Optoelectron. Rev.* **2002**, *10*, 237–242.
163. Forghani, K.; Guan, Y.; Wood, A.W.; Anand, A.; Babcock, S.E.; Mawst, L.J.; Kuech, T.F. Self-limiting growth when using trimethyl bismuth (TMBi) in the metal-organic vapor phase epitaxy (MOVPE) of $GaAs_{1-y}Bi_y$. *J. Cryst. Growth* **2014**, *395*, 38–45. [CrossRef]
164. Kaminska, M.; Weber, E.; Liliental-Weber, Z.; Leon, R.; Rek, Z. Stoichiometry-related defects in GaAs grown by molecular-beam epitaxy at low temperatures. *J. Vac. Sci. Technol. B Microelectron. Process. Phenom.* **1989**, *7*, 710–713. [CrossRef]
165. Ludewig, P.; Bushell, Z.; Nattermann, L.; Knaub, N.; Stolz, W.; Volz, K.O. Growth of Ga(AsBi) on GaAs by continuous flow MOVPE. *J. Cryst. Growth* **2014**, *396*, 95–99. [CrossRef]

166. Ludewig, P.; Knaub, N.; Stolz, W.; Volz, K. MOVPE growth of Ga(AsBi)/GaAs multi quantum well structures. *J. Cryst. Growth* **2013**, *370*, 186–190. [CrossRef]
167. Liu, H.; Wang, T.; Jiang, Q.; Hogg, R.; Tutu, F.; Pozzi, F.; Seeds, A. Long-wavelength InAs/GaAs quantum-dot laser diode monolithically grown on Ge substrate. *Nat. Photonics* **2011**, *5*, 416–419. [CrossRef]
168. Wang, T.; Lee, A.; Tutu, F.; Seeds, A.; Liu, H.; Jiang, Q.; Groom, K.; Hogg, R. The effect of growth temperature of GaAs nucleation layer on InAs/GaAs quantum dots monolithically grown on Ge substrates. *Appl. Phys. Lett.* **2012**, *100*, 052113. [CrossRef]
169. Lee, A.; Jiang, Q.; Tang, M.; Seeds, A.; Liu, H. Continuous-wave InAs/GaAs quantum-dot laser diodes monolithically grown on Si substrate with low threshold current densities. *Opt. Express* **2012**, *20*, 22181–22187. [CrossRef]
170. Chen, S.; Li, W.; Wu, J.; Jiang, Q.; Tang, M.; Shutts, S.; Elliott, S.N.; Sobiesierski, A.; Seeds, A.J.; Ross, I. Electrically pumped continuous-wave III–V quantum dot lasers on silicon. *Nat. Photonics* **2016**, *10*, 307–311. [CrossRef]
171. Han, C.; Zheng, Z.; Shu, H.; Jin, M.; Qin, J.; Chen, R.; Tao, Y.; Shen, B.; Bai, B.; Yang, F. Slow-light silicon modulator with 110-GHz bandwidth. *Sci. Adv.* **2023**, *9*, eadi5339. [CrossRef] [PubMed]
172. Ma, Y.; Zhao, J.; Yang, T.; Mei, Y.; Sun, Z.; Lu, J.; Li, S.; Ma, X.; Chen, X. Hybrid-integrated 200 Gb/s REC-DML array transmitter based on photonic wire bonding technology. *Chin. Opt. Lett.* **2024**, *22*, 081401. [CrossRef]
173. Tian, W.; Wang, Y.; Dang, H.; Hou, H.; Xi, Y. Photonic integrated circuits: Research advances and challenges in interconnection and packaging technologies. *Photonics* **2025**, *12*, 821. [CrossRef]
174. Wang, C.; Li, Z.; Riemensberger, J.; Lihachev, G.; Churaev, M.; Kao, W.; Ji, X.; Zhang, J.; Blesin, T.; Davydova, A. Lithium tantalate photonic integrated circuits for volume manufacturing. *Nature* **2024**, *629*, 784–790. [CrossRef]
175. Asadizanjani, N.; Reddy Kottur, H.; Dalir, H. CVD in Semiconductor Packaging. In *Introduction to Microelectronics Advanced Packaging Assurance*; Springer: Berlin/Heidelberg, Germany, 2025; pp. 41–60.
176. Sun, Y.; Yin, R.; Zhang, J.; Liu, J.; Fei, T.; Li, K.; Guo, K.; Jia, Z.; Liu, S.; Lu, Q. High-performance quantum cascade lasers at λ∼9 μm grown by MOCVD. *Opt. Express* **2022**, *30*, 37272–37280. [CrossRef]
177. Bekman, H.T.; Van Den Heuvel, J.; Van Putten, F.; Schleijpen, R. Development of a mid-infrared laser for study of infrared countermeasures techniques. In *Technologies for Optical Countermeasures*; SPIE: Bremerhaven, Germany, 2004; pp. 27–38.
178. Botez, D.; Kirch, J.D.; Boyle, C.; Oresick, K.M.; Sigler, C.; Kim, H.; Knipfer, B.B.; Ryu, J.H.; Lindberg, D., III; Earles, T. High-efficiency, high-power mid-infrared quantum cascade lasers. *Opt. Mater. Express* **2018**, *8*, 1378–1398. [CrossRef]
179. Corrigan, P.; Martini, R.; Whittaker, E.A.; Bethea, C. Quantum cascade lasers and the Kruse model in free space optical communication. *Opt. Express* **2009**, *17*, 4355–4359. [CrossRef]
180. Curl, R.F.; Capasso, F.; Gmachl, C.; Kosterev, A.A.; McManus, B.; Lewicki, R.; Pusharsky, M.; Wysocki, G.; Tittel, F.K. Quantum cascade lasers in chemical physics. *Chem. Phys. Lett.* **2010**, *487*, 1–18. [CrossRef]
181. Phillips, M.C.; Bernacki, B.E.; Harilal, S.S.; Yeak, J.; Jones, R.J. Standoff chemical plume detection in turbulent atmospheric conditions with a swept-wavelength external cavity quantum cascade laser. *Opt. Express* **2020**, *28*, 7408–7424. [CrossRef]
182. Sun, Y.; Yang, K.; Liu, J.; Zhang, J.; Zhuo, N.; Liu, J.; Liu, S.; Wang, L.; Liu, F.; Zhai, S. High sensitivity and fast detection system for sensing of explosives and hazardous materials. *Sens. Actuators B Chem.* **2022**, *360*, 131640. [CrossRef]
183. Wang, F.; Slivken, S.; Razeghi, M. High-brightness LWIR quantum cascade lasers. *Opt. Lett.* **2021**, *46*, 5193–5196. [CrossRef] [PubMed]
184. Xie, F.; Caneau, C.; Leblanc, H.P.; Caffey, D.P.; Hughes, L.C.; Day, T.; Zah, C.-E. Watt-level room temperature continuous-wave operation of quantum cascade lasers with λ > 10 μm. *IEEE J. Sel. Top. Quantum Electron.* **2013**, *19*, 1200407.
185. Razeghi, M.; Bai, Y.; Wang, F. High-power, high-wall-plug-efficiency quantum cascade lasers with high-brightness in continuous wave operation at 3–300 μm. *Light Sci. Appl.* **2025**, *14*, 252. [CrossRef]
186. Han, Y.; Chen, W.; Jiao, T.; Yu, H.; Zhang, Z.; Dong, X.; Zhang, Y.; Zhang, B. Silicon-based gallium oxide optical waveguide fabricated by MOCVD. *Vacuum* **2025**, *238*, 114221. [CrossRef]
187. Al-Ezzi, A.S.; Ansari, M.; Tan, N. Flexible and freestanding solar cells based on metal organic chemical vapour deposition-grown graphene. *Chem. Pap.* **2025**, *79*, 2019–2036. [CrossRef]
188. Teloeken, A.; Lamb, D.; Dunlop, T.; Irvine, S. Effect of bending test on the performance of CdTe solar cells on flexible ultra-thin glass produced by MOCVD. *Sol. Energy Mater. Sol. Cells* **2020**, *211*, 110552. [CrossRef]
189. Arifin, P.; Subagio, A.; Sutanto, H.; Dwiputra, D.; Florena, F.F.; Keintjem, A.C.; Khaeroni, R. Room-temperature photoluminescence of Mg-doped GaN thin films grown by plasma-assisted MOCVD. *AIP Adv.* **2020**, *10*, 045123. [CrossRef]
190. Dhara, S.; Dheenan, A.; Kalarickal, N.K.; Huang, H.-L.; Islam, A.E.; Joishi, C.; Fiedler, A.; McGlone, J.F.; Ringel, S.A.; Hwang, J. Plasma-assisted deposition and characterization of Al_2O_3 dielectric layers on (001) β-Ga_2O_3. *Appl. Phys. Lett.* **2023**, *123*, 083504. [CrossRef]
191. Hasan, S.; Mamun, A.; Hussain, K.; Gaevski, M.; Ahmad, I.; Khan, A. Growth evolution of high-quality MOCVD aluminum nitride using nitrogen as carrier gas on the sapphire substrate. *J. Mater. Res.* **2021**, *36*, 4360–4369. [CrossRef]
192. Kwak, H.-M.; Kim, J.; Lee, J.-S.; Kim, J.; Baik, J.; Choi, S.-Y.; Shin, S.; Kim, J.-S.; Mun, S.-H.; Kim, K.-P. 2D-material-assisted GaN growth on GaN template by MOCVD and its exfoliation strategy. *ACS Appl. Mater. Interfaces* **2023**, *15*, 59025–59036. [CrossRef]

193. Meng, L.; Yu, D.; Huang, H.-L.; Chae, C.; Hwang, J.; Zhao, H. MOCVD growth of β-Ga_2O_3 on (001) Ga_2O_3 substrates. *Cryst. Growth Des.* **2024**, *24*, 3737–3745. [CrossRef]
194. Wang, B.; Zeng, Y.; Song, Y.; Wang, Y.; Liang, L.; Qin, L.; Zhang, J.; Jia, P.; Lei, Y.; Qiu, C. Principles of Selective Area Epitaxy and Applications in III–V Semiconductor Lasers Using MOCVD: A Review. *Crystals* **2022**, *12*, 1011. [CrossRef]
195. Wong, M.S.; Speck, J.S.; Nakamura, S.; DenBaars, S.P. Progress in III-nitride tunnel junctions for optoelectronic devices. *IEEE J. Quantum Electron.* **2022**, *58*, 1–11. [CrossRef]
196. Wu, J.; Li, L.; Wang, X.; Wang, C.; Yao, G.; Luo, Z.; Feng, L.; Liu, H.; Li, S.; Gao, F. Advances in gallium nitride/two-dimensional-material heterojunction-based photodetectors. *Inf. Funct. Mater.* **2025**, *2*, 172–215. [CrossRef]
197. Ahn, J.-H. 2D MoS_2 Thin-Film Transistors for Large-Area, Flexible Electronics. In Proceedings of the 2025 9th IEEE Electron Devices Technology & Manufacturing Conference (EDTM), Hong Kong, China, 9–12 March 2025; pp. 1–3.
198. Cai, Y.; He, Y.; Wang, G.; Li, Z.; Pei, Y.; Yang, W.; Rao, W.; Li, J. Machine learning models in the process of metal organic chemical vapor deposition epitaxial manufacturing of Gallium Arsenide. *Mater. Today Commun.* **2024**, *40*, 109808. [CrossRef]
199. Momeni, K.; Ji, Y.; Nayir, N.; Sakib, N.; Zhu, H.; Paul, S.; Choudhury, T.H.; Neshani, S.; Van Duin, A.C.; Redwing, J.M. A computational framework for guiding the MOCVD-growth of wafer-scale 2D materials. *npj Comput. Mater.* **2022**, *8*, 240. [CrossRef]
200. Chen, L.-R.; Hong, K.-B.; Huang, K.-C.; Liu, C.-L.; Lin, W.; Lu, T.-C. Study of an epitaxial regrowth process by MOCVD for photonic-crystal surface-emitting lasers. *Cryst. Growth Des.* **2021**, *21*, 3521–3527. [CrossRef]
201. Shi, B.; Koscica, R.; Skipper, A.; Brunelli, S.S.; Leake, G.J.; Herman, J.; Harame, D.; Bowers, J.; Dummer, M.; Klamkin, J. Scalable and Monolithic Integration of Quantum Dot Lasers for Silicon Photonics. In Proceedings of the 2025 Optical Interconnects and Packaging Conference (OIP), Fort Collins, CO, USA, 16–18 June 2025; pp. 1–2.
202. Zhang, X.; Trainor, N.; Mc Knight, T.V.; Graves, A.R.; Wu, Z.; Xu, L.; Zheng, X.; Zhang, T.; Zhu, J.; Palacios, T. Metal–organic chemical vapour deposition for 2D chalcogenides. *Nat. Rev. Methods Primers* **2025**, *5*, 57. [CrossRef]

Disclaimer/Publisher's Note: The statements, opinions and data contained in all publications are solely those of the individual author(s) and contributor(s) and not of MDPI and/or the editor(s). MDPI and/or the editor(s) disclaim responsibility for any injury to people or property resulting from any ideas, methods, instructions or products referred to in the content.